Table 2. Comparison of GANP expression in various CNS tumors by IHC

Samples	No. of cases	GANP expression†			
		−	±	+	++
PCNSL	25	1	6	4	14
AA	10	1	4	4	1
GBM	20	3	11	6	0
Medulloblastoma	4	3	0	1	0

†Relative expression level of germinal center–associated nuclear protein (GANP) by immunohistochemical (IHC) score. AA, anaplastic astrocytoma; CNS, central nervous system; GBM, glioblastoma multiforme; PCNSL, primary central nervous system lymphoma.

tumor specimens. Paraffin sections (4-μm) were immunostained with rat antimouse GANP monoclonal antibody (mAb)[13] in combination with biotinylated antirat IgG Ab with Vectastain ABC complex (Vector Laboratories, Burlingame, CA, USA) and 3,3-diaminobenzidine (Sigma-Aldrich, St. Louis, MO, USA). The staining intensity was evaluated by two investigators as IHC score as follows: −, negative; ±, weak; +, intermediate; ++, strong.

Real-time RT-PCR. PCR was performed using a LightCycler (Roche Molecular Biochemicals, Indianapolis, IN, USA). Specific oligonucleotide primers and probes for *ganp* and glyceraldehyde-3-phosphate dehydrogenase (*gapdh*) were purchased (Nihon Gene Research Laboratories, Sendai, Japan). The level of *ganp* mRNA expression is determined in comparison with that of *gapdh*. Primers and probes are listed in Table 1.

Cell culture, transfection, and irradiation (IR). MRC-5 and five human MG cell lines, U251MG, U373MG, T98G, U87MG, and A172, were maintained in DMEM (Invitrogen, Carlsbad, CA, USA) supplemented with 10% fetal calf serum (Sigma-Aldrich), 2 mM L-glutamine (Cambrex, East Rutherford, NJ, USA), and 5×10^{-5} M 2-mercaptoethanol with 5% CO_2 at 37°C. Cells were transfected with 10 nM (final concentration) of the small interfering RNA (siRNA) using Lipofectamine RNAiMAX (Invitrogen). Stealth RNAi duplexes (Invitrogen) are listed in Table 1. Exposure to IR was done using Gamma-cell 40 extracter (Nordion International, Ottawa, ON, Canada) with a ^{137}Cs source.

Cell-cycle analysis. The siRNA-treated cells were collected, washed with PBS, and incubated with propidium iodide (PI) solution.[18] For bromodeoxyuridine (BrdU) incorporation analysis, siRNA-treated cells were labeled with 10 μM BrdU before harvest. DNA was stained with 7-amino-actinomycin D and fluorescein isothiocyanate (FITC)-conjugated anti-BrdU Ab using the FITC BrdU Flow Kit (BD Biosciences, San Jose, CA, USA). The cell cycle was analyzed using FACSCalibur (BD, Franklin Lakes, NJ, USA) with the CellQuest software.

Senescence-associated β-galactosidase (SA-β-gal) staining. SA-β-gal activity was detected with a Senescence β-Galactosidase Staining Kit (Cell Signaling, Danvers, MA, USA).

Immunoblotting and immunofluorescence. Cells were treated with siRNA or irradiation and lysed by TNE buffer and the cell lysates were separated by SDS-PAGE followed by immunoblotting.[13] Primary Abs against GANP,[13] p53 (Calbiochem, San Diego, CA, USA), p16 (BD Biosciences), p21 (Santa Cruz Biotechnology, Santa Cruz, CA, USA), and Rb (BD Biosciences) were used in comparison with β-actin Ab (a loading control). Cells were fixed with 3.7% paraformaldehyde and incubated with anti-trimethyl-Histone H3 (Lys9) Ab (Millipore, Bedford, MA, USA) and Alexa488-conjugated goat antirabbit IgG (Invitrogen).[18] To detect the nuclei, cells were fixed with 3.7% paraformaldehyde, permeabilized by 0.2% Triton X-100, and stained with PI.

Table 3. Comparison of *ganp* mRNA expression with clinicopathologic features in MGs

Factor	No. of cases	*Ganp* mRNA (Mean ± SD)	Mann–Whitney *U*-test *P*-values
Age (years)			
>50	58	8 ± 7	0.0020*
≤50	43	15 ± 12	
Sex			
Male	58	11 ± 9	0.8260
Female	43	12 ± 12	
Histological type			
AA (WHO grade III)**	29	19 ± 13	<0.0001*
GBM (WHO grade IV)	72	8 ± 6	
Preop KPS Score (%)			
>70	87	11 ± 10	0.5946
≤70	14	11 ± 14	
MIB-1 LI (%)			
>20	35	9 ± 8	0.0019*
≤20	66	14 ± 12	
Non-tumor brain	4	15 ± 3	n.d.

*The statistical significances are shown. **AA was selected from World Health Organization (WHO) grade III in this comparison. AA, anaplastic astrocytoma; GBM, glioblastoma multiforme; LI, labeling index; MGs, malignant gliomas; n.d., not determined; preop KPS score, preoperative Karnofsky Performance Scale score; SD, standard deviation.

Table 4. Multivariate analyses of prognostic factors in MGs

Factor	OS		PFS	
	HR (95% CI)	*P*-values	HR (95% CI)	*P*-values
Age (>50/≤50)	0.36 (0.20–0.64)	<0.01*	1.01 (0.48–2.10)	0.98
WHO grade (III/IV)	10.74 (3.99–28.94)	<0.01*	2.51(1.18–5.31)	0.01*
MIB-1 LI (>20/≤20)	1.16 (0.71–1.91)	0.54	0.63 (0.32–1.27)	0.19
ganp expression (≥10/<10)	1.02 (0.56–1.84)	0.95	0.48 (0.22–1.05)	0.06

*The statistical significances are shown. CI, confidence interval; *ganp*, germinal center–associated nuclear protein; HR, hazard ratio; LI, labeling index; MGs, malignant gliomas; WHO, World Health Organization.

Fluorescence *in situ* hybridization (FISH). U251MG cells treated with siRNA were incubated with colcemid (0.02 μg/mL) for 4 h, harvested, re-suspended in 0.075 M KCl, and fixed in 3:1 methanol/glacial acetic acid. The centromeric region-specific FISH probes for human chromosomes were prepared using two bacterial artificial chromosomes RP11-88E13 and RP11-164B7 by labeling with digoxigenin-11-dUTP (for chromosome 7) and dinitrophenyl-11-dUTP (for chromosome 9), respectively. Cells were incubated with the mixed probes with Cy3-labeled anti-digoxigenin and Cy5-labeled anti-dinitrophenyl Abs in comparison with 4,6-diamino-2-phenylindole staining. The images were captured with the CW4000 FISH application program (Leica Microsystems Imaging Solution, Cambridge, UK).

Statistical analyses. The non-parametric Mann–Whitney *U*-test was adopted for statistical analysis of the association between *ganp* mRNA expression and clinicopathologic factors. Overall survival (OS) and progression-free survival (PFS) curves were prepared by Kaplan–Meier method and verified by the log-rank (Mantel–Cox) test. The independent effect of each parameter on OS and PFS was analyzed using the multivariate Cox proportional hazards regression model. The difference was considered significant when a *P*-value of <5% was obtained.

Results

Decreased expression of GANP in MGs. GANP expression occurs at high levels in various human hematological disorders including Hodgkin's lymphoma, acute myeloid leukemia, and myelodysplastic syndrome.[18] *Ganp*-Tg mice develop Hodgkin-like lymphomas at high incidence, which confirmed the association between increased GANP expression and tumorigenesis.[18] Here, we examined the expression of GANP in various CNS tumors by using IHC (Fig. 1a, Table 2). GANP was expressed at high levels in primary CNS lymphomas (PCNSL), but at rather lower ones in the malignant tumors of AA, GBM, and medulloblastoma. The larger magnification images were shown in the lower panel. Thus, we examined the expression of *ganp* mRNA in 101 cases of MGs (29 cases of AA and 72 cases of GBM) and four cases of non-tumor brain by quantitative real-time RT-PCR as the relative copy number in comparison with the control *gapdh* mRNA (Table 3). The non-tumor brain tissues showed the expression of *ganp* mRNA at 15 copies in the average. In MGs, the *ganp* mRNA was at seven copies as the median value (between 0 and 58 copies). The cases were divided into two groups by age (≤50 years and >50 years), sex, the histological type of AA and GBM corresponding to World Health Organization (WHO) grade III and IV, respectively, preoperative Karnofsky Performance Scale (KPS) score (<70 and ≥70), or MIB-1 LI (<20 and ≥20). The expression of *ganp* mRNA did not show any significant difference in the comparison by sex or preoperative KPS score; however, it differed significantly in the comparison by age, WHO grade, or MIB-1 LI. The level of *ganp* mRNA was significantly lower in the case of patients >50 years of age, GBM (WHO grade IV), or high MIB-1 LI; and the difference was marked in the comparison by WHO grade. The GBM group showed significantly lower expression of *ganp* mRNA (8 ± 6) than AA (grade III; 19 ± 13; $P < 0.0001$). This observation suggests that decreased expression of *ganp* mRNA might be associated with the malignant character of tumors.

A clinically meaningful cut-off point for *ganp* mRNA expression was determined for the comparison between the expression and the post-operative survival time by using the Kaplan–Meier method and log-rank (Mantel–Cox) test. A remarkable difference was observed when the cases were compared at the cut-off point of 10 copies, with the cases being classified into $ganp^{Low}$ (<10) and $ganp^{High}$ (≥10) groups. The $ganp^{Low}$ patient group showed significantly worse survival than the $ganp^{High}$ group in terms of the OS rate ($P < 0.0001$) and in terms of the PFS rate ($P = 0.0018$, Fig. 1b). To assess the association of survival duration with multiple clinical characteristics (age, WHO grade, MIB-1 LI, and *ganp* mRNA expression), we performed multivariate analysis (Table 4). Age and WHO grade were found to be independent prognostic factors for OS, but the decrease of *ganp* mRNA expression was not an independent prognostic factor for OS and PFS.

Association of LOH10 and *EGFR* amplification with the decreased expression of GANP in MGs. To investigate further the relevance of low *ganp* expression to the development of gliomas, we compared the existence of LOH10[3] and *EGFR* amplification[4] between the $ganp^{Low}$ and the $ganp^{High}$ glioma groups. LOH10 appeared in 69% of $ganp^{Low}$ cases, which was much higher ($P = 0.0274$) than the 44% for the $ganp^{High}$ cases (Fig. 1c, *left*). *EGFR* amplification was detected in 31% of $ganp^{Low}$ cases, which was four times higher ($P = 0.0161$) than the 7% for the $ganp^{High}$ ones (Fig. 1c, right). The decrease in *ganp* mRNA expression thus appears to be an indicator of the poor prognosis of MGs.

Effect of decreased GANP expression on cell proliferation and cell-cycle progression of human diploid fibroblast cells. To examine whether a decrease in GANP expression causes abnormal cell growth, we treated human diploid fibroblast MRC-5 cells with a siRNA for *ganp*. The *ganp* siRNA markedly suppressed the expression of *ganp* transcripts compared with the control siRNA as assessed by real-time RT-PCR (Fig. 2a, left) and this suppression was confirmed by immunoblotting (Fig. 2a, right). Next, the cells were examined by cell-cycle analysis after BrdU incorporation (Fig. 2b). Treatment with *ganp* siRNA caused remarkable cell-cycle abnormalities after 2 days, i.e., an increase in the number of mitotic cells and a decrease in that of S-phase cells, and no alteration in that of apoptotic cells, as determined by flow cytometric analysis (Fig. 2b). Another set of *ganp* siRNA (*ganp* siRNA2) also suppressed *ganp* expression and caused the similar cell-cycle change, indicating that the cell-cycle change was really induced by the suppression of GANP (Fig. 2c). *Ganp* RNA interference (RNAi)-treatment of MRC-5 cells caused a marked increase in the number of SA-β-gal$^+$ cells compared with that obtained with control siRNA-treated cells (Fig. 2d). MRC-5 cells showed the cell-cycle arrest of the cellular-senescence phenotype after *ganp* RNAi-treatment. Cellular senescence induced after *ganp* RNAi-treatment was caused by prolonged cell-cycle arrest with activation of p16 and the decrease of Rb expression similar to those caused by 6-Gy irradiation (Fig. 2b,e). We confirmed that cellular senescence had occurred in *ganp* siRNA-treated cells, by analyzing senescence-associated heterochromatin foci (SAHF) as another feature of cellular senescence.[22] K9M-H3, a marker of SAHF[22], appeared as typical punctate regions of DNA corresponding to heterochromatic foci in *ganp* siRNA-treated cells (Fig. 2f).

Effect of decreased GANP expression in MG cell lines harboring genetic abnormalities. Five MG cell lines (Table 4), U251MG, U373MG, U87MG, T98G, and A172, carrying various genetic abnormalities showed cell-cycle abnormalities with various degrees of hyperploidy after anti-microtubule drug (AMD) treatment.[23–25] In contrast with the case of MRC-5 fibroblasts, *ganp* RNAi-treatment caused remarkable cell-cycle abnormalities in U251MG cells, with an increase in the percentage of mitotic cells (from 15.2% to 23.3%) and hyperploid cells (from 1.36% to 15.6%) at day 5, as determined by flow cytometric analysis (Fig. 3a, left). On the contrary, U87MG cells showed no significant change in the generation of hyperploid cells (from 5.08% to 6.41%) after the same treatment; whereas G2/M-phase cells increased (from 25.2% to 31.9%; Fig. 3a, right). This result indicates that *ganp* RNAi-treatment caused the hyperploidy in U251MG in a cell-type specific manner. A peculiar difference between U251MG and U87MG cells is the p53 state. U251MG carries a *p53* mutation, whereas U87MG has the wild-type (WT) *p53*.[23] Immunoblot analysis showed that the level of WT p53 was increased in *ganp* siRNA-treated U87MG, indicating that the cell-cycle checkpoint governed by p53 operated normally in this cell line (Fig. 3b). The mutant p53 might allow the mitotic slippage of U251MG cells undergoing DDR.[24] U87MG and A172 carrying WT p53 did not show any increase in the percentage of hyperploid cells; whereas the other cell lines carrying p53 mutations, U251MG, U373MG, and T98G, generated more hyperploid cells (Table 5).

Induction of CIN by *ganp* RNAi-treatment in MG cell lines that harbor p53 mutations. *Ganp* RNAi-treatment generated large nuclei with abnormal contours in U251MG cells but not in U87MG ones, as detected by PI staining (Fig. 3c, arrows). We further examined whether *ganp* RNAi-treatment would cause increases in CIN and the number of *EGFR* genes as in glioma cells.[26–30] The hyperploidy was examined by using FISH to detect the multiplicity of chromosome 7 carrying the *EGFR* gene and chromosome 9 (Fig. 3d). Typically in control siRNA-treated U251MG cells, there were more than two copies of chromosome 7 (red);[24] however, *ganp* RNAi-treatment increased the number of chromosomes to over 10 signals per cell (Fig. 3). These results indicate that the decrease in the level of *ganp* mRNA resulted in cell-cycle abnormali-

doi: 10.1111/j.1349-7006.2009.01293.x

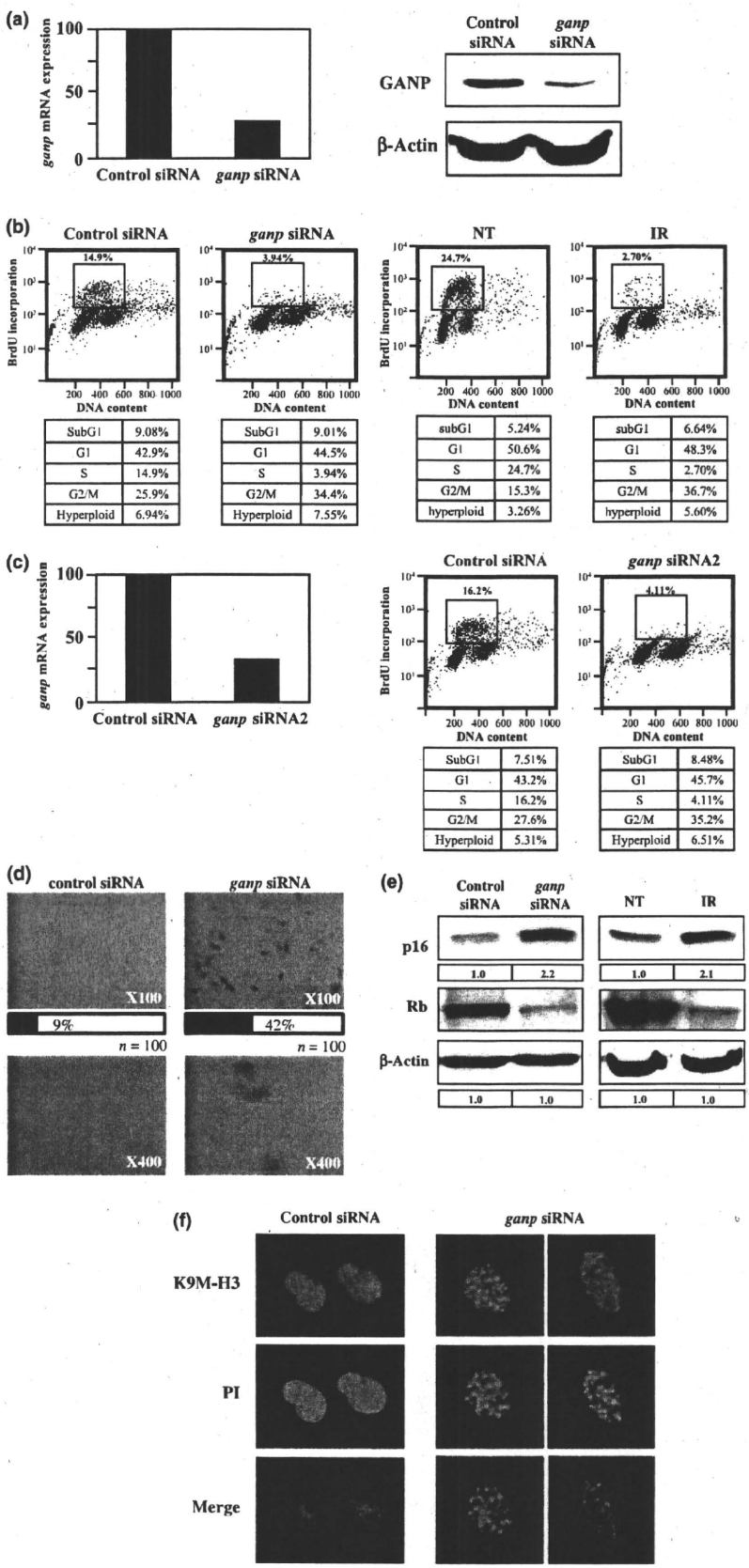

Fig. 2. Induction of cellular senescence by germinal center–associated nuclear protein (*ganp*) RNA interference (RNAi)-treatment in human diploid fibroblast. (a, left panel) Suppression of GANP by *ganp* RNAi-treatment. *Ganp* mRNA was examined by real-time PCR in siRNA-treated MRC-5 after 48 h. *Ganp* mRNA is shown as the arbitrary copy in comparison with *gapdh* mRNA. (right panel) GANP protein was examined by immunoblot analysis. β-Actin was used as a loading control. (b) Effect of RNAi-treatment or irradiation (IR) on MRC-5 was examined by cell-cycle analysis. Cell-cycle distribution was examined by BrdU incorporation on the *x*-axis with the total DNA content on the *y*-axis. Box indicates cells in the S-phase. (c, left panel) Another sequence of *ganp* RNAi-treatment (*ganp* siRNA2) in human diploid fibroblast. Suppression of *ganp* transcription in *ganp* siRNA2-treated cells. *Ganp* mRNA was examined by real-time PCR in *ganp* siRNA2-treated MRC-5 after 48 h. *Ganp* mRNA is shown as the arbitrary copy in comparison with *gapdh* mRNA. (right panel) Cell-cycle analysis in *ganp* siRNA2-treated cells. Cell-cycle distribution was examined by BrdU incorporation on the *x*-axis with the total DNA content on the *y*-axis. Box indicates cells in the S-phase. (d) Induction of SA-β-gal activity in MRC-5 after *ganp* RNAi-treatment. Images of low (×100) and high (×400) magnification are shown in control or *ganp* siRNA-treated cells. Percentages indicate the number of SA-β-gal$^+$ cells per 100 cells. (e) Expression of cell cycle–related molecules in MRC-5 after *ganp* RNAi- or IR-treatment. Cell lysates from MRC-5 treated with siRNA or IR were subjected to immunoblotting with the Abs. (f) Induction of SAHF in MRC-5 after *ganp* RNAi-treatment. MRC-5 were stained with anti-trimethyl-Histone H3 (Lys9) (K9M-H3) Ab and viewed under a fluorescent microscope. Counterstaining was done by propidium iodine (PI).

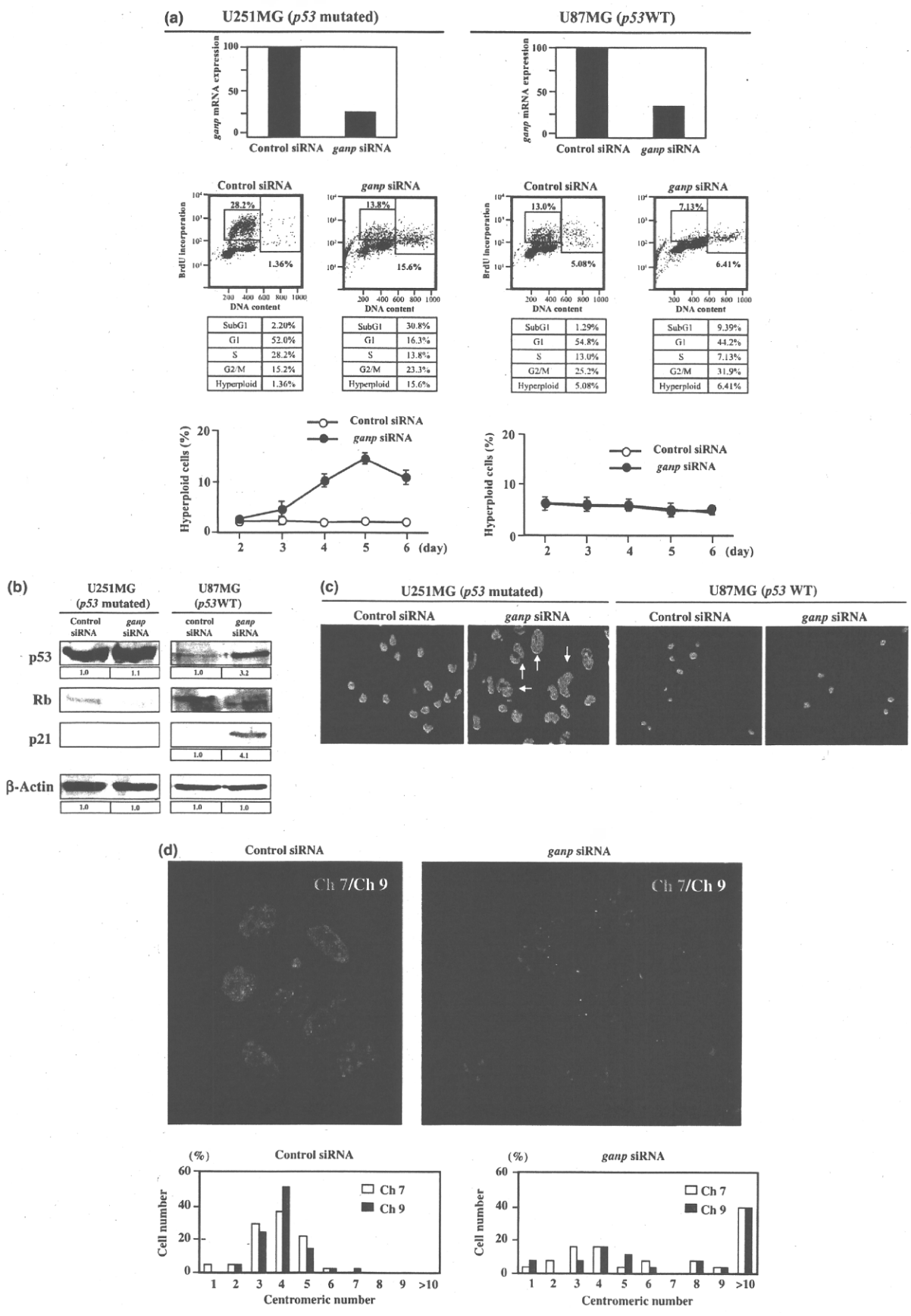

doi: 10.1111/j.1349-7006.2009.01293.x

Table 5. Effect of *ganp* siRNA on various malignant glioma cell lines

Cell line	Gene state†		Hyperploid cell (%)‡	
	p53	*p16*	Control siRNA	*ganp* siRNA
U251MG	Mutated	Deleted	1.84 ± 0.23	16.5 ± 0.85
U87MG	WT	Deleted	4.57 ± 0.69	5.43 ± 1.08
U373MG	Mutated	Deleted	1.58 ± 0.08	17.2 ± 1.05
T98G	Mutated	Deleted	2.40 ± 0.31	21.0 ± 0.53
A172	WT	Deleted	1.91 ± 0.59	1.13 ± 0.11

†Gene states were obtained from a previous report.[43] ‡Hyperploid cells were calculated by flow cytometry after 5 days of RNA interference (RNAi)-treatment. *ganp*, germinal center–associated nuclear protein.

ties generating hyperploid cells, in association with another genetic abnormality (in this case, the p53 mutation) of cell-cycle control.

Discussion

In this study, we focused on the expression of GANP in MGs with a poor prognosis and studied the molecular mechanism to explain how the low *ganp* expression is associated with the generation of CIN in MG cell lines. Our results demonstrated that the expression of GANP, a putative component of the ribonucleoprotein complex, is significantly decreased in the group of MGs with poor prognosis.

The formation of mature ribonucleoprotein particles probably plays a role not only in gene expression, but also in the maintenance of genome stability.[31] Null mutation of any component of suppressor of the Transcriptional defects of Hpr1Δ by Overexpression (THO) results in similar phenotypes of transcription impairment and defects in mRNA export. Analysis of THO mutants in yeast led to the hypothesis that transcription-associated hyper-recombination is tightly linked to transcriptional-elongation impairment and is presumably caused by the co-transcriptional formation of R-loops (DNA–RNA hybrids).[32]

We examined how the decrease in the GANP level affected cell-cycle progression and generated hyperploidy in MG cell lines of different genetic abnormalities; and based on our results we propose a model to show how GANP insufficiency is associated with malignant progression of MGs (Fig. 4). The lack of p53 results not only in the DNA damage-induced impairment of checkpoints but also in the impairment of the spindle assembly checkpoint, and cells lacking p53 become hyperploid after treatment with AMD.[33,34] GANP insufficiency causes cells to initiate DDR. When the DNA damage is irreparable, cells undergo apoptosis or cellular senescence (Fig. 4a). However, MG cells harboring various genetic abnormalities may become hyperploid by the decreased expression of GANP under the G1-checkpoint abrogation that leads to the continuation of cell cycling as mitotic slippage (Fig. 4b). The MG cell lines harboring WT p53 did not generate hyperploid cells by inhibiting cell-cycle progression at the G2/M-phase after the DDR, suggesting that the critical gatekeeper is p53 in the transcription-coupled DDR.

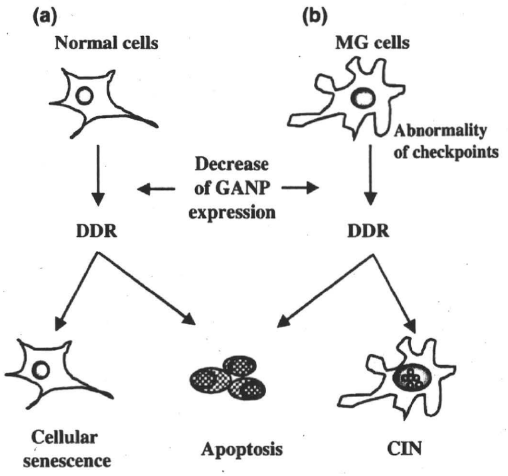

Fig. 4. A proposed model regarding germinal center–associated nuclear protein (GANP) insufficiency and malignant progression of malignant gliomas (MGs). GANP insufficiency causes normal or malignant cells to initiate DNA damage response (DDR). In case of irreparable DNA damages, normally cells cause apoptosis or cellular senescence accompanied with up-regulation of p16 (a). Adversely, MG cells harboring various genetic abnormalities including p53 mutation may generate hyperploid cells by GANP insufficiency under the G1-checkpoint abrogation that leads to the continuation of cell cycling as mitotic slippage (b).

Cells with DNA damage normally undergo cell-cycle arrest at the G2-phase, owing to the intact G2 checkpoint. These cells undergo cellular senescence without further progression of the cell cycle. GANP insufficiency causes a continuous cell-cycle arrest and generates cellular-senescence changes, although it may not be a direct cause of oncogenesis under the intact checkpoint regulation.

The senescence response appears to be due to either one or both of the two pathways leading to senescent cell-cycle arrest, which are governed by tumor suppressor proteins p53 and Rb.[35,36] The inhibitor of CDKs (INK) proteins including $p16^{INK4a}$ specifically inhibit the activity of cyclin D-dependent kinases to prevent the phosphorylation of Rb family proteins.[37,38] The $p16^{INK4a}$-Rb pathway controls the cell cycle at the G1-phase and induces cell-cycle arrest as replicative senescent cells, which are represented by the development of dense foci of heterochromatin.[22,39] Treatment with *ganp* siRNA markedly augmented the expression of p16 and prevented the phosphorylation of Rb, indicating that the DDR caused by GANP insufficiency was mediated by the $p16^{INK4a}$-Rb pathway.

The transcription of the *ganp* gene is regulated by the E2F consensus element (at -56 bp in the mouse).[40] The E2F transcription factor plays a pivotal role in the timely activation of gene expression during mammalian cell-cycle progression.[41] Co-expression of E2F-2 and p53 enhances the anti-cancer effect of p53 in glioma cells.[42] The critical elements associated with

Fig. 3. Induction of hyperploid cells by germinal center–associated nuclear protein (*ganp*) RNA interference (RNAi -treatment in human malignant glioma (MG)cell lines. (a, upper panel) Suppression of *ganp* transcription by *ganp* RNAi-treatment. *Ganp* mRNA was examined by real-time RT-PCR in U251MG and U87MG after 48 h of RNAi-treatment. *Ganp* mRNA is shown as the arbitrary copy in comparison with *gapdh* mRNA. (middle panel) Effect of RNAi-treatment on U251MG and U87MG was examined by cell-cycle analysis after 5 days. Cell-cycle distribution was examined by BrdU incorporation on the *x*-axis and total DNA content on the *y*-axis. Left box, cells in the S-phase; right box, cells in hyperploid cells with DNA content larger than 4N. (lower panel) Line graphs summarizing the percentage of hyperploid cells with more than 4N DNA content were measured over a 6-day period using two cell lines. (b) Expression of cell cycle–related molecules in MG cell lines after *ganp* RNAi-treatment. Cell lysates from U251MG and U87MG treated with siRNA were subjected to immunoblotting with Abs. (c) DNA staining of U251MG and U87MG was performed after RNAi-treatment. Arrows indicate large nucleated cells in comparison with control siRNA-treated cells (magnification, ×400). (d, upper panel) Dual-color FISH analysis of U251MG after RNAi-treatment. U251MG treated with siRNA were examined after 5 days by FISH using fluorescent probes for chromosome 7 (red) and 9 (yellow) (magnification, ×1000). (lower panel) The centromeric copy number was scored by examining more than 50 cells.

tumorigenesis and malignant progression of MG cases need to be determined.

In conclusion, we have herein shown that down-regulation of GANP caused cellular senescence in fibroblast cells and also caused CIN in association with a p53 abnormality in MGs.

Acknowledgments

This work was supported by Grant-in-Aid from the Ministry of Education, Culture, Sports, Science and Technology of Japan; CREST of JST; and the Advanced Education Program for Integrated Clinical, Basic and Social Medicine, Graduate School of Medical Sciences, Kumamoto University. We thank Dr. Masahisa Tsuji for dual-color FISH and Ms. Masako Obata for technical assistance.

Disclosure Statement

There is no conflict of interest for any of the authors.

References

1 Zhu Y, Parada LE. The molecular and genetic basis of neurological tumours. *Nat Rev Cancer* 2002; **2**: 616–26.
2 The Cancer Genome Atlas Research Network. Comprehensive genomic characterization defines human glioblastoma genes and core pathways. *Nature* 2008; **455**: 1061–8.
3 Tada K, Shiraishi S, Kamiryo T *et al.* Analysis of loss of heterozygosity on chromosome 10 in patients with malignant astrocytic tumors: correlation with patient age and survival. *J Neurosurg* 2001; **95**: 651–9.
4 Shinojima N, Tada K, Shiraishi S *et al.* Prognostic value of epidermal growth factor receptor in patients with glioblastoma multiforme. *Cancer Res* 2003; **63**: 6962–70.
5 Reifenberger G, Liu L, Ichimura K, Schmidt EE, Collins VP. Amplification and overexpression of the MDM2 gene in a subset of human malignant gliomas without *p53* mutations. *Cancer Res* 1993; **53**: 2736–9.
6 Albertson DG, Collins C, McCormick F, Gray JW. Chromosome aberrations in solid tumors. *Nat Genet* 2003; **34**: 369–76.
7 Di Micco R, Fumagalli M, d'Adda di Fagagna F. Breaking news: high-speed race ends in arrest – how oncogenes induce senescence. *Trends Cell Biol* 2007; **17**: 529–36.
8 Svejstrup JQ. Mechanisms of transcription-coupled DNA repair. *Nat Rev Mol Cell Biol* 2002; **3**: 21–9.
9 Gaillard H, Wellinger RE, Aguilera A. A new connection of mRNP biogenesis and export with transcription-coupled repair. *Nucleic Acids Res* 2007; **35**: 3893–906.
10 Fischer T, Strasser K, Racz A *et al.* The mRNA export machinery requires the novel Sac3p-Thp1p complex to dock at the nucleoplasmic entrance of the nuclear pores. *EMBO J* 2002; **21**: 5843–52.
11 Gallardo M, Luna R, Erdjument-Bromage H, Tempst P, Aguilera A. Nab2p and the Thp1p-Sac3p complex functionally interact at the interface between transcription and mRNA metabolism. *J Biol Chem* 2003; **278**: 24225–32.
12 Aguilera A. Cotranscriptional mRNP assembly: from the DNA to the nuclear pore. *Curr Opin Cell Biol* 2005; **17**: 242–50.
13 Kuwahara K, Yoshida M, Kondo E *et al.* A novel nuclear phosphoprotein, GANP, is up-regulated in centrocytes of the germinal center and associated with MCM3, a protein essential for DNA replication. *Blood* 2000; **95**: 2321–8.
14 Kuwahara K, Fujimura S, Takahashi Y *et al.* Germinal center-associated nuclear protein contributes to affinity maturation of B cell antigen receptor in T cell-dependent responses. *Proc Natl Acad Sci USA* 2004; **101**: 1010–5.
15 Sakaguchi N, Kimura T, Matsushita S *et al.* Generation of high-affinity antibody against T cell-dependent antigen in the *ganp* gene-transgenic mouse. *J Immunol* 2005; **174**: 4485–94.
16 Kuwahara K, Tomiyasu S, Fujimura S *et al.* Germinal center-associated nuclear protein (GANP) has a phosphorylation-dependent DNA primase activity that is up-regulated in germinal center regions. *Proc Natl Acad Sci USA* 2001; **98**: 10279–83.
17 Takei Y, Swietlik M, Tanoue A, Tsujimoto G, Kouzarides T, Laskey R. MCM3AP, a novel acetyltransferase that acetylates replication protein MCM3. *EMBO Rep* 2001; **2**: 119–23.
18 Fujimura S, Xing Y, Takeya M *et al.* Increased expression of germinal center-associated nuclear protein RNA-primase is associated with lymphomagenesis. *Cancer Res* 2005; **65**: 5925–34.
19 Yoshida M, Kuwahara K, Shimasaki T, Nakagata N, Matsuoka M, Sakaguchi N. GANP suppresses DNA recombination, measured by direct-repeat β-*galactosidase* gene construct, but does not suppress the type of recombination applying to immmunoglobulin genes in mammalian cells. *Genes Cells* 2007; **12**: 1205–13.
20 Shiraishi S, Tada K, Nakamura H *et al.* Influence of p53 mutations on prognosis of patients with glioblastoma. *Cancer* 2002; **95**: 249–57.
21 Kamiryo T, Tada K, Shiraishi S *et al.* Analysis of loss of homozygous deletion of the p16 gene and correlation with survival in patients with glioblastoma multiforme. *J Neurosurg* 2002; **96**: 815–22.
22 Narita M, Nunez S, Heard E *et al.* Rb-mediated heterochromatin formation and silencing of E2F target genes during cellular senescence. *Cell* 2003; **113**: 703–16.
23 Nitta M, Tsuiki H, Arima Y *et al.* Hyperploidy induced by drugs that inhibit formation of microtubule promotes chromosome instability. *Genes Cells* 2002; **7**: 151–62.
24 Tsuiki H, Nitta M, Tada M *et al.* Mechanism of hyperploid cell formation induced by microtubule inhibiting drug in glioma cell lines. *Oncogene* 2001; **20**: 420–9.
25 Hong FD, Chen J, Donovan S *et al.* Taxol, vincristine or nocodazole induces lethality in G1-checkpoint-defective human astrocytoma U373MG cells by triggering hyperploid progression. *Carcinogenesis* 1999; **20**: 1161–8.
26 Nishizaki T, Harada K, Kubota H *et al.* Chromosomal instability in malignant astrocytic tumors detected by fluorescence *in situ* hybridization. *J Neurooncol* 2002; **56**: 159–65.
27 Nishizaki T, Kubota H, Harada K *et al.* Clinical evidence of distinct subgroups of astrocytic tumors defined by comparative genomic hybridization. *Hun Pathol* 2000; **31**: 608–14.
28 Lengauer C, Kinzler KW, Vogelstein B. Genetic instabilities in human cancers. *Nature* 1998; **396**: 643–9.
29 Saito T, Hama S, Izumi H *et al.* Centrosome amplification induced by survivin suppression enhances both chromosome instability and radiosensitivity. *Br J Cancer* 2008; **98**: 345–55.
30 Inoue T, Hiratsuka M, Osaki M *et al.* SIRT2, a tubulin deacetylase, acts to block the entry to chromosome condensation in response to mitotic stress. *Oncogene* 2007; **26**: 945–57.
31 Luna R, Jimeno S, Marín M, Huertas P, García-Rubio M, Aguilera A. Interdependence between transcription and mRNP processing and export, and its impact on genetic stability. *Mol Cell* 2005; **18**: 711–22.
32 Huertas P, Aguilera A. Cotranscriptionally formed DNA:RNA hybrids mediate transcription elongation impairment and transcription-associated recombination. *Mol Cell* 2003; **12**: 711–21.
33 Di Leonardo A, Khan SH, Linke SP *et al.* DNA rereplication in the presence of mitotic spindle inhibitors in human and mouse fibroblasts lacking either p53 or pRb function. *Cancer Res* 1997; **57**: 1013–9.
34 Khan SH, Wahl GM. p53 and pRb prevent rereplication in response to microtubule inhibitors by mediating a reversible G1 arrest. *Cancer Res* 1998; **58**: 396–401.
35 Finkel T, Serrano M, Blasco MA. The common biology of cancer and aging. *Nature* 2007; **448**: 767–74.
36 Mooi WJ, Peeper DS. Oncogene-induced cell senescence-halting on the road to cancer. *N Engl J Med* 2006; **355**: 1037–46.
37 Ruas M, Peters G. The p16INK4a/CDKN2A tumor suppressor and its relatives. *Biochim Biophys Acta* 1998; **1378**: F115–77.
38 Sherr CJ, Roberts JM. CDK inhibitors: positive and negative regulators of G1-phase progression. *Genes Dev* 1999; **13**: 1501–12.
39 Zhang R, Poustovoitov MV, Ye X *et al.* Formation of MacroH2A-containing senescence-associated heterochromatin foci and senescence driven by ASF1a and HIRA. *Dev Cell* 2005; **8**: 19–30.
40 EL-Gazzar MA, Maeda K, Nomiyama H, Nakao M, Kuwahara K, Sakaguchi N. PU.1 is involved in the regulation of B lineage-associated and developmental stage-dependent expression of the germinal center-associated DNA primase GANP. *J Biol Chem* 2001; **276**: 48000–8.
41 Takahashi Y, Rayman JB, Dynlacht BD. Analysis of promoter binding by the E2F and pRB families in vivo: distinct E2F proteins mediate activation and progression. *Genes Dev* 2000; **14**: 804–16.
42 Mitlianga PG, Kyritsis AP, Gomez-Manzano C *et al.* Co-expression of E2F-2 enhances the p53 anti-cancer effect in human glioma cells. *Int J Oncol* 2001; **18**: 343–7.
43 Wang C-C, Liao Y-P, Mischel PS, Iwamoto KS, Cacalano NA, McBride WH. HDJ-2 as target for radiosensitization of glioblastoma multiforme cells by the farnesyltransferase inhibitor R115777 and the role of the p53/p21 pathway. *Cancer Res* 2006; **66**: 6756–62.

doi: 10.1111/j.1349-7006.2009.01293.x

European Journal of Radiology 73 (2010) 532–537

Contents lists available at ScienceDirect

European Journal of Radiology

journal homepage: www.elsevier.com/locate/ejrad

Glioblastoma treated with postoperative radio-chemotherapy: Prognostic value of apparent diffusion coefficient at MR imaging

Fumiyuki Yamasaki[a], Kazuhiko Sugiyama[a], Megu Ohtaki[b], Yukio Takeshima[c], Nobukazu Abe[d], Yuji Akiyama[d], Junko Takaba[d], Vishwa Jeet Amatya[c], Taiichi Saito[a], Yoshinori Kajiwara[a], Ryosuke Hanaya[a], Kaoru Kurisu[a,*]

[a] Department of Neurosurgery, Graduate School of Biomedical Sciences, Hiroshima University, Hiroshima 1-2-3 Kasumi, Minami-ku, Hiroshima 734-8551, Japan
[b] Department of Environmetrics and Biometrics, Research Institute for Radiation Biology and Medicine, Hiroshima University, Hiroshima, Japan
[c] Department of Pathology, Graduate School of Biomedical Sciences, Hiroshima University, Hiroshima, Japan
[d] Department of Radiology, Graduate School of Biomedical Sciences, Hiroshima University, Hiroshima, Japan

ARTICLE INFO

Article history:
Received 9 September 2008
Received in revised form 7 January 2009
Accepted 7 January 2009

Keywords:
Apparent diffusion coefficient
Echo planar imaging
Glioblastoma
Magnetic resonance imaging
Overall survival

ABSTRACT

Purpose: To retrospectively evaluate whether the mean, minimum, and maximum apparent diffusion coefficient (ADC) of glioblastomas obtained from pretreatment MR images is of prognostic value in patients with glioblastoma.

Materials and methods: The institutional review board approved our study and waived the requirement for informed patient consent. Between February 1998 and January 2006, 33 patients (24 males, 9 females; age range 10–76 years) with supratentorial glioblastoma underwent pretreatment magnetic resonance (MR) imaging. The values of the mean, minimum, and maximum ADC (ADC_{mean}, ADC_{MIN}, and ADC_{MAX}, respectively) of each tumor were preoperatively determined from several regions of interest defined in the tumors. After surgical intervention, all patients underwent irradiation and chemotherapy performed according to our hospital protocol. The patient age, symptom duration, Karnofsky performance scale score, extent of surgery, and ADC were assessed using factor analysis of overall survival. Prognostic factors were evaluated using Kaplan–Meier survival curves, the log-rank test, and multiple regression analysis with the Cox proportional hazards model.

Results: Likelihood ratio tests confirmed that ADC_{MIN} was the strongest among the three prognostic factors. Total surgical removal was the most important predictive factor for overall survival ($P<0.01$). ADC_{MIN} was also statistically correlated with overall survival ($P<0.05$) and could be used to classify patients into different prognostic groups. Interestingly, ADC_{MIN} was also the strongest prognostic factor ($P<0.01$) in the group of patients in whom total tumor removal was not possible.

Conclusion: The ADC_{MIN} value obtained from pretreatment MR images is a useful clinical prognostic biomarker in patients with glioblastoma.

1. Introduction

Glioblastoma is the most common malignant primary neoplasm of the central nervous system; median survival is approximately 1 year [1,2]. Conventional magnetic resonance imaging (MRI) can yield information on the gross anatomic structure of glioblastoma, but it provides little functional information. Diffusion-weighted (DW) MRI enables the volumetric intravoxel measurement of tissue characteristics based on the detection of changes in the random motion of water protons at the cellular or physiological level [3]. Although the usefulness of DW-MRI for preoperative grading and postoperative assessment of glial tumors has been investigated [4–7], its value for predicting survival has not been fully addressed [8–10]. Because the apparent diffusion coefficient (ADC) is inversely related to tumor cellularity and the glioma grade [4,6,11–14], we postulated that it reflects the biological viability and prognosis of glioblastomas. We therefore analyzed the ADC with respect to the surgical resection status and compared the mean, minimum, and maximum ADC (ADC_{mean}, ADC_{MIN}, and ADC_{MAX}, respectively) values as factors reflecting biological activity. We performed a retrospective study to determine whether these values obtained on preoperative MRI scans are of prognostic value in patients with glioblastoma. We discovered that the ADC_{MIN} value is a prognostic factor for survival in patients with glioblastomas that are not totally resectable.

* Corresponding author. Tel.: +81 82 257 5227; fax: +81 82 257 5229.
E-mail address: kuka422@hiroshima-u.ac.jp (K. Kurisu).

0720-048X/$ – see front matter © 2009 Elsevier Ireland Ltd. All rights reserved.
doi:10.1016/j.ejrad.2009.01.013

2. Materials and methods

The institutional review board of our hospital approved this retrospective study and waived the requirement for informed patient consent. Patient information was kept confidential by removing all identifiers from our records at the completion of our analyses.

3. Patients, diagnosis and treatment

Between February 1998 and January 2006, 49 patients (29 males, 20 females) with histologically confirmed supratentorial glioblastoma were treated at our institution. Of these, 16 were excluded from this study for reasons such as incomplete MRI, progression from anaplastic or low-grade glioma, infratentorial tumors, and incomplete- or no postoperative irradiation or chemotherapy. The remaining 33 patients (24 males, 9 females; age range 10–76 years) with new, histologically confirmed glioblastoma who underwent pretreatment MRI were included in this study. Maximum tumor resection was performed in all patients; it was followed by postoperative external-beam radiation therapy and chemotherapy. Histopathological diagnoses based on World Health Organization criteria were determined by consensus between two authors (V.J.A., Y.T.) who were blinded to the MRI results. Gadolinium-enhanced MRI performed within 1 week after surgery was used to categorize the surgical results according to the removed tumor proportion, i.e., biopsy, ≤50%; partial removal, 50–95%; subtotal removal, 96–99%; total removal, >99%. Nitrosourea-based chemotherapy and radiation therapy were administered concurrently. Patients were followed up to evaluate tumor control after postoperative radiation therapy. Follow-up included physical and neurological examinations and MRI study. Salvage surgery, additional radiation therapy, and/or chemotherapy were considered in patients with tumor recurrence or progression.

4. MRI study and image interpretation

All MRI scans were performed using a 1.5-T superconducting system (Signa Horizon; GE Medical Systems, Milwaukee, WI, USA) with a circularly polarized head coil. All patients underwent MRI studies that included at least unenhanced and contrast-enhanced transverse T1-weighted-, unenhanced transverse T2-weighted-, unenhanced transverse fluid-attenuated inversion-recovery (FLAIR)-, and unenhanced transverse DW images. The transverse T1-weighted spin–echo MR sequence was performed using the following parameters: repetition time ms/echo time ms, 400/8; field of view (FOV), 22 cm × 16 cm; matrix size, 256 (frequency), 192 (phase); section thickness, 5 mm; section gap, 2.5 mm; two signals were acquired. The contrast-enhanced T1-weighted sequences were obtained after administering 0.1 mmol of gadodinium compound per kg body weight. The transverse fast spin–echo T2-weighted sequence was performed using the following parameters: 3500/100; FOV, 22 cm × 16 cm; matrix size, 256 × 192; echo train length, 12; section thickness, 5 mm; section gap, 2.5 mm; 2 signals. Transverse FLAIR images were acquired using fast and interleaved multi-section sequences with the following parameters: 10,000/150; inversion time, 2200 ms; FOV, 22 cm × 22 cm; matrix size, 256 × 192; echo train length, 16; section thickness, 5 mm; section gap, 2.5 mm; 1 signal. Transverse DW images were acquired using a single-shot T2-weighted echo planar spin–echo sequence before contrast-enhanced T1-weighted imaging. We calculated ADC values according to the formula $ADC = -[\ln(Sb/S0)]/b$, where Sb is the signal intensity (SI) of the region of interest (ROI) obtained through three orthogonally oriented DW images, $S0$ the SI of the ROI acquired through reference T2-weighted images, and b is the gradient b factor with a value of 1000 s/mm^2. ADC maps were calculated on a pixel-by-pixel basis using software integral to the MR unit. The ADC was measured by manually placing ROI in tumor regions on the ADC map at the site of enhanced lesions on contrast-enhanced T1-weighted MRI. Cystic components were differentiated as areas of hyperintensity on T2-weighted- and hypointensity on FLAIR MRI scans. Necrotic components were differentiated on contrast-enhanced T1-weighted images as the interior of enhanced lesions. Hemorrhagic lesions were identified on unenhanced T1-weighted MRI as areas of hyperintensity and on unenhanced T2-weighted MRI as areas of hypointensity. We compared the ADC maps and other MR images, being careful to manually place the ROI only in the solid tumor components. Based on 6–10 ROI ranging in size from 40 to 60 mm^2 on the ADC maps, we obtained ADC_{mean}, ADC_{MIN}, and ADC_{MAX}, respectively. We performed DWI using the following parameters: before July 2003: 1600/107; diffusion gradient encoding in 3 (x, y, z) orthogonal directions; b values of 250, 500, 750, and 1000 s/mm^2; FOV, 24 cm × 24 cm; matrix size, 128 × 128; section thickness, 7.5 mm; section gap, 0 mm; one signal. After July 2003 the parameters were: 5000/107; diffusion gradient encoding in 3 (x, y, z) orthogonal directions; b values of 1000 s/mm^2; FOV, 24 cm × 24 cm; matrix size, 128 × 128; section thickness, 7.5 mm; section gap, 0 mm; 1 signal.

5. Statistical analyses

Survival was measured from the time of operation to the time of death or last follow-up (range, 3.6–54.4 months; median, 16.6 months). Of the 33 patients, 6 were alive at the time of the latest follow-up. We used the median of ADC_{mean}, ADC_{MIN}, and ADC_{MAX} as the cutoff value. We also applied a categorization cutoff of 1.0×10^{-3} mm^2/s because earlier studies used this value [4,10]. We analyzed the relationship between patient survival and prognostic factors determined from clinical and MRI data. Prognostic factors included the patient age, gender, duration of symptoms, Karnofsky performance scale (KPS) score, extent of surgery (biopsy, partial, subtotal or total resection) and ADC ($>1.0 \times 10^{-3}$ vs. $\leq 1.0 \times 10^{-3}$ mm^2/s). Survival curves were calculated with the Kaplan–Meier method, the log-rank test was used to analyze overall differences in the survival curves. The influence of prognostic factors was adjusted using multiple regression analysis with the Cox proportional hazards model. We applied the likelihood ratio test to make comparisons among ADC_{mean}, ADC_{MIN}, and ADC_{MAX} as prognostic factors. All statistical analyses were performed using computer software (StatView version 5.0; SAS

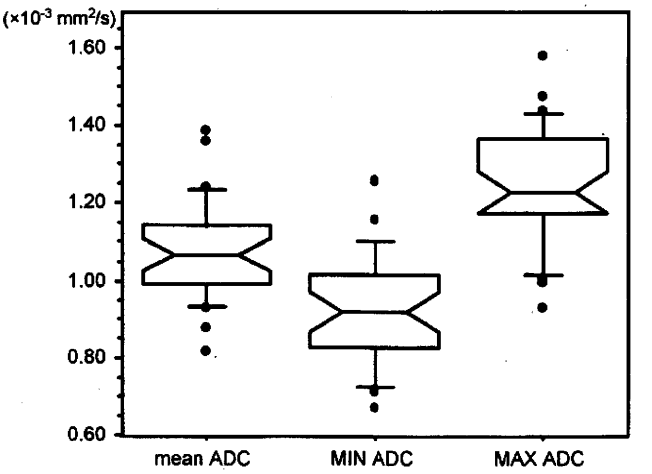

Fig. 1. Parallel boxplots showing the distribution of mean, minimum and maximum ADC values for all glioblastoma patients.

Table 1
Univariate analysis of specific prognostic factors.

Prognostic factor	No. of patients (n=33)	Overall survival[a]	P-value[†]
Age (year)			
≤49	8	37.5%	NA
≥50	25	40.0%	
Sex			
Male	24	41.7%	NA
Female	9	33.3%	
Symptom duration (month)			
≤3	25	36.0%	NA
>3	8	50.0%	
Karnofsky performance score			
≥80	23	47.8%	<0.05
≤70	10	20.0%	
Extent of surgery			
Total	7	71.4%	<0.01
Not total (subtotal, partial and biopsy)	26	30.8%	
Apparent diffusion coefficient			
≤1.00 ($\times 10^{-3}$ mm^2/s)	23	30.4%	<0.05
>1.00 ($\times 10^{-3}$ mm^2/s)	10	60.0%	

[a] Data are 1.5-year overall survival rates, expressed as percentages. The 1.5-year overall survival rate for all 33 patients was 39.4% (13 patients).
[†] P-values calculated with the log-rank test. NA, not applicable; hazard ratio not calculated when $P \geq 0.05$.

Institute, Cary, NC). For all statistical tests, $P < 0.05$ was adopted as the significance level.

6. Results

6.1. Patient characteristics and imaging

The patients ranged in age from 10 to 76 years (mean ± standard deviation (S.D.): 57.3 ± 16.3; median 62). The KPS scores were 30 and 50 in 1 patient each, 60 and 70 in 4 each, 80 in 11, 90 in 9, and 100 in 3 patients. Surgery consisted of biopsy (n=6), partial- (n=12), subtotal- (n=8), and total (n=7) tumor removal. The ADC_{mean} of all tumors ranged from 0.716×10^{-3} to 1.389×10^{-3} mm^2/s (mean ± S.D. $1.070 \pm 0.141 \times 10^{-3}$ mm^2/s; median 1.066×10^{-3} mm^2/s). The ADC_{MIN} ranged from 0.676×10^{-3} to 1.260×10^{-3} mm^2/s (mean ± S.D. $0.934 \pm 0.144 \times 10^{-3}$ mm^2/s; median, 0.933×10^{-3} mm^2/s). The ADC_{MAX} ranged from 0.935×10^{-3} to 1.585×10^{-3} mm^2/s (mean ± S.D. $1.248 \pm 0.151 \times 10^{-3}$ mm^2/s; median, 1.230×10^{-3} mm^2/s) (Fig. 1). There was no statistical difference under our two imaging conditions.

6.2. Comparison among ADC_{mean}, ADC_{MIN}, and ADC_{MAX} values by likelihood ratio analysis

We initially performed comparisons among ADC_{mean}, ADC_{MIN}, and ADC_{MAX} values to identify the most powerful prognostic factor

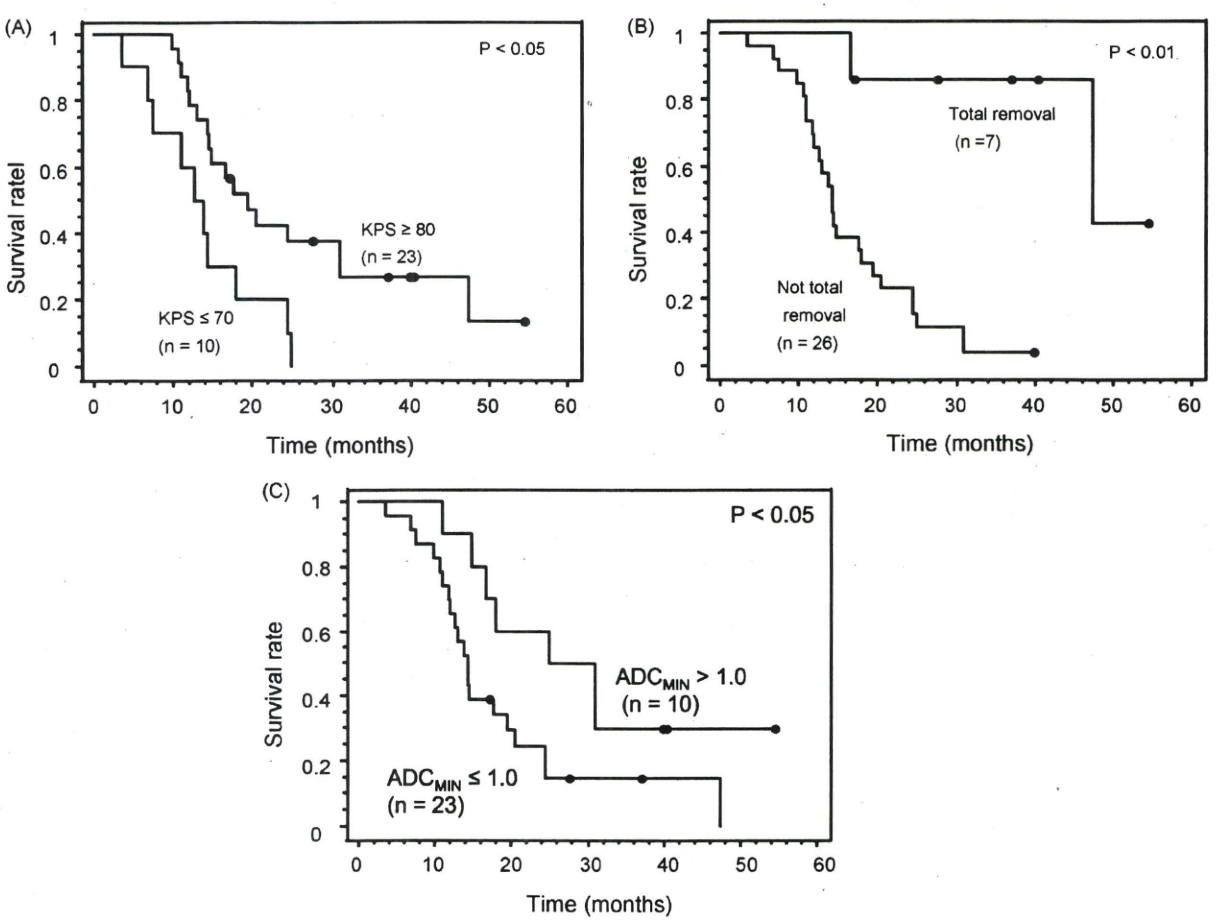

Fig. 2. Kaplan–Meier survival curves for all patients with glioblastoma (including six who remain alive) showing the relationship between minimum ADC and survival time measured from the date of surgery. Comparisons were done between KPS ≥80 and KPS ≤70 (A), between total and not total removal (B), and between ADC > 1.0×10^3 and ≤1.0×10^3 mm^2/s (C).

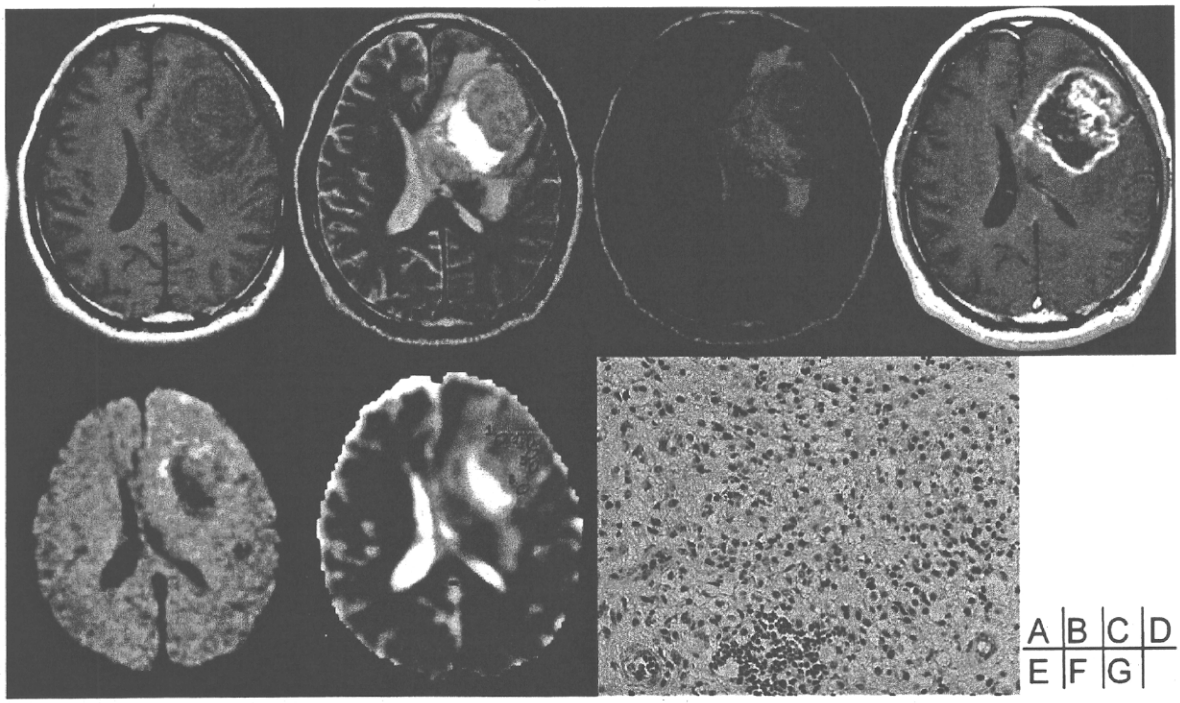

Fig. 3. MR images and pathological results obtained in 60-year-old man with glioblastoma. (A) T1-weighted-, (B) T2-weighted-, (C) FLAIR-, (D) contrast-enhanced T1-weighted images show an enhancing tumor and peritumoral edema. (E) On the DW image, the enhancing area exhibits moderately high signal intensity. (F) On the ADC map, the enhancing area manifests a minimum ADC of 1.05×10^{-3} mm^2/s. The tumor was partially removed and this patient survived for 31 months after the initial MRI study. (G) Histologic specimen (160×) shows the mildly hypercellular nature of the tumor.

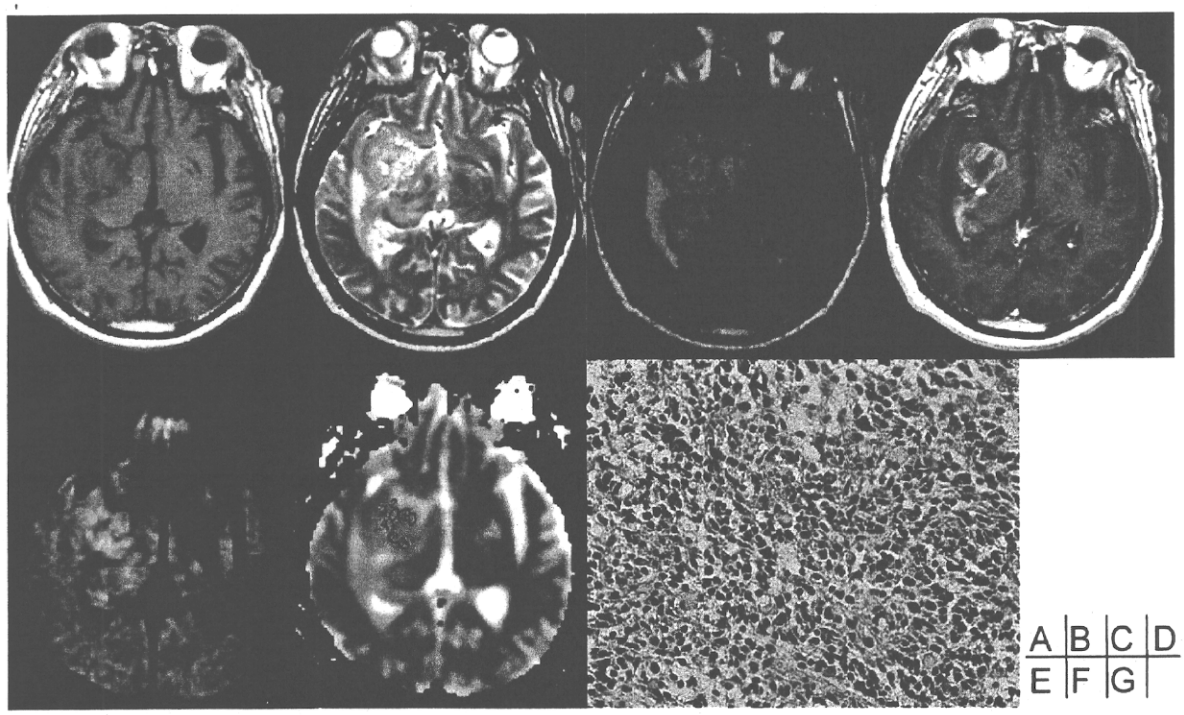

Fig. 4. Transverse MR images obtained in 67-year-old man with glioblastoma. (A) T1-weighted-, (B) T2-weighted-, and (C) FLAIR image. (D) Contrast-enhanced T1-weighted images show an enhancing tumor. (E) On the DW image, the enhancing area exhibits high signal intensity. (F) On the ADC map, the enhancing area has a minimum ADC of 0.902×10^{-3} mm^2/s. The tumor was subtotally removed and this patient died 13 months after the initial MRI study. (G) Histologic specimen (160×) shows marked hypercellularity of the tumor.

Table 2
Multivariate analysis of specific prognostic factors.

Prognostic factor	Hazard ratio	*P*-value
Age (≥50)	NA	NA
Gender	NA	NA
Symptom duration (≤3.0 months)	NA	NA
KPS score (≤70)	NA	NA
Extent of resection (not total)	19.187	<0.01
Minimum ADC ($\leq 1.0 \times 10^{-3}$ mm²/s)	3.915	<0.05

NA, not applicable; hazard ratio not calculated when $P \geq 0.05$.

according to likelihood ratio analysis (Fig. 1). We analyzed the ADC with surgical results because "total removal" was the most sensitive prognostic factor according to our analyses. The results of likelihood ratio analysis were ADC_{mean}, $\chi^2 = 16.291$ ($P = 0.003$); ADC_{MIN}, $\chi^2 = 19.739$ ($P < 0.0001$), and ADC_{MAX}, $\chi^2 = 13.633$ ($P = 0.0011$). Based on these findings we used ADC_{MIN} in further analyses.

6.3. Univariate analyses of prognostic factors

Univariate analysis (Table 1) revealed that the significant factors in overall survival were the KPS score ($P < 0.05$) (Fig. 2A), total surgical removal ($P < 0.01$; Fig. 2B), and ADC_{MIN} ($P < 0.05$; Figs. 2C, 3, and 4). Other factors were not associated with overall survival. Among our 33 patients, the ADC_{MIN} value was below 1.0×10^{-3} mm²/s in 23; it was higher in 10 patients. The group-specific survival rate at 1.5 years was 30.4% and 60.0% for patients in the low- and high ADC_{MIN} value groups, respectively ($P < 0.05$; Fig. 2C).

6.4. Multivariate analysis of prognostic factors

We evaluated the prognostic factors for overall survival using multivariate analysis. The results of multiple regression analysis with the Cox proportional hazards model (Table 2) confirmed that incomplete tumor removal was the most important prognostic factor (hazard ratio 19.187; $P < 0.01$). Our results also confirmed that a low ADC_{MIN} value was a statistical prognostic factor (hazard ratio 3.915; $P < 0.05$). No other factors were significantly associated with overall survival.

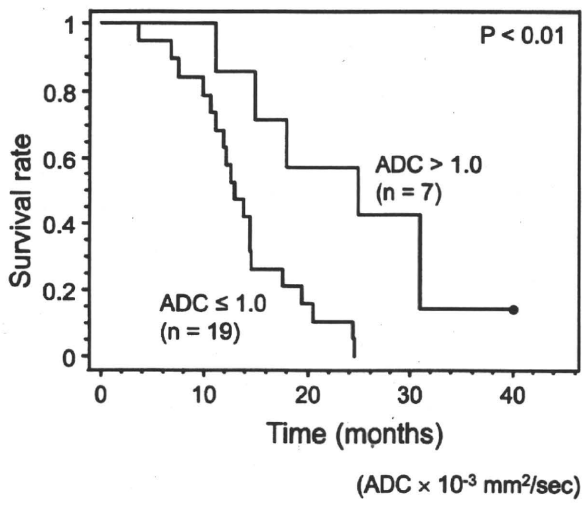

Fig. 5. Kaplan–Meier survival curves based on minimum ADC ($>1.0 \times 10^3$ vs. $\leq 1.0 \times 10^3$ mm²/s) in the subgroup of patients with incomplete tumor removal.

6.5. Survival analysis of patients with incomplete tumor removal

We analyzed the prognostic factors in patients whose tumors could not be totally removed because the biological features of post-operative residual tumors may affect overall survival. Univariate analysis with the log-rank test revealed that the only significant factor for overall survival was the ADC_{MIN} ($P < 0.01$; Fig. 5). Neither the patient age (≥50 year) nor the gender, symptom duration (≤3.0 months), KPS (≥80), subtotal tumor removal, nor surgical achievements were of prognostic value. The results of multivariate analysis with the Cox proportional hazards model also confirmed that low ADC_{MIN} was a powerful prognostic factor (hazard ratio 6.107, $P < 0.01$).

7. Discussion

Our results suggest that the ADC value of tumors, obtained from preoperative MRI scans, represents a prognostic factor in patients with glioblastoma. Although ADC_{mean}, ADC_{MIN}, and ADC_{MAX} were statistically significant prognostic factors in our patients, we confirmed that ADC_{MIN} was the most sensitive predictive factor for the overall survival of these patients. Others [9,10] who assessed the value of the ADC for predicting the prognosis of patients with malignant astrocytic tumors used ADC_{MIN} based on the hypothesis that this value reflects the sites of highest cellularity within heterogeneous tumors and that these sites are of prognostic importance. Studies of ADC that documented an inverse relationship between tumor cellularity and the glioma grade support this hypothesis [6,11,12]. Tissues with high cellularity manifest a low ADC because the mobility of water protons is impeded; cystic and necrotic regions, on the other hand, exhibit a high ADC due to the rapid diffusion of water protons [13,15]. However, no previous reports have compared the value of the ADC_{MIN} versus the ADC_{mean} and ADC_{MAX}. Our likelihood ratio analysis confirmed that ADC_{MIN} was the most sensitive prognostic factor and that it can be used to evaluate overall survival in patients with glioblastoma.

Our observation that a low ADC_{MIN} value is associated with a poor prognosis is consistent with previous studies. According to Higano et al. [9] who studied 37 patients with malignant astrocytic tumors including 22 glioblastomas, the outcomes were more favorable in groups with $ADC_{MIN} > 0.90 \times 10^{-3}$ mm²/s than $\leq 0.90 \times 10^{-3}$ mm²/s [9]. We also applied the cutoff values of 0.90×10^{-3} mm²/s of ADC_{MIN} and of the median 0.933×10^{-3} mm²/s (median of ADC_{MIN}) in our statistical analyses. At both cutoff values, groups with a lower ADC had a statistically poorer prognosis ($P < 0.01$, log-rank test; data not shown) and our results agree with their findings. Higano et al. [9] also found a significant negative correlation between ADC_{MIN} and the Ki-67 labeling index; this may explain why the group with the lower ADC_{MIN} value had a poor prognosis. Murakami et al. [10] studied 79 malignant supratentorial astrocytic tumors, including 50 glioblastomas; patients whose $ADC_{MIN} > 1.00 \times 10^{-3}$ mm²/s had better outcomes than patients with $ADC_{MIN} \leq 1.00 \times 10^{-3}$ mm²/s, a value they considered the most important factor in predicting a poor prognosis (hazard ratio 10.459). Although they did not provide information regarding the degree of surgical resection, our results coincide with theirs. Our findings and those of others confirm that the ADC_{MIN} statistically correlates with the prognosis of glioblastoma patients.

In our series, total, but not subtotal removal or less affected overall survival; an observation that coincides with that of others [16]. Interestingly, we found that the ADC_{MIN} of tumors on pretreatment MR images was a useful predictor of the overall survival of glioblastoma patients whose tumors could not be totally removed. Oh et al. [8] who evaluated the ADC_{mean} of glioblastomas on MR images obtained after surgery but before the start of radiation therapy

found that the survival of patients with a low ADC was substantially shorter. Our findings support their results.

In combination with conventional MRI findings, the ADC can yield additional useful information about physiological changes since the entire tumor can be assessed. Tissue sampling, on the other hand, may not yield information about the entire tumor. Furthermore, if the chosen biopsy site is suboptimal, the glioma grading may be incorrect because these tumors are histologically heterogeneous. Thus, because the ADC helps to identify areas of highest cellularity within a tumor, it is useful for selecting the biopsy target [9].

Our study has some limitations. DWI does not eliminate perfusion effects attributable to tumor vessels or white matter tracts. In addition, ADC changes due to cystic, necrotic, and/or hemorrhagic areas and the influence of artifacts caused by inhomogeneous structures such as the skull base, bone, and sinus air must be considered. To avoid the influence of susceptibility artifacts or ADC changes, we excluded patients with infratentorial tumors or gross hemorrhage from our study. Another limitation was the variability of the calculated ADC. Significant variability in ADC values reportedly reflects the coil systems and imagers used, the instrument vendors, and the field strengths applied for MR re-imaging [17,18]. We set the cut off value of ADC_{MIN} at 1.00×10^{-3} mm^2/s and this value would be affected, therefore, we suggest that the optimal absolute ADC be established by larger studies. The semiquantitative use of the ADC such as its ratio to the contralateral side, may help to eliminate these variabilities. However, as the ADC is inhomogenous in various brain lesions and is affected by aging [19–21], these ADC changes must be considered when the ratio to the contralateral normal-appearing side is to be established. Future studies are necessary to standardize ADC measurement methods. Although our retrospective study showed that ADC_{MIN} is one of the most important prognostic factors, due to the heterogeneous nature of glioblastomas, other variables related to the characteristics of the patients, the tumors, and the treatment strategies must be taken into account.

8. Conclusions

The ADC_{MIN} value of tumors obtained from preoperative MR images is a useful clinical prognostic biomarker for overall survival in patients with glioblastoma. Patients whose tumors have a low minimum ADC ($\leq 1.0 \times 10^{-3}$ mm^2/s) may have a poor prognosis, especially when the tumor cannot be completely resected. Thus, pretreatment DW-MRI and calculating the ADC values may be helpful for planning therapy in patients with glioblastoma.

Conflicts of interest

None.

References

[1] DeAngelis LM. Brain tumors. N Engl J Med 2001;344(2):114–23.
[2] Behin A, Hoang-Xuan K, Carpentier AF, Delattre JY. Primary brain tumours in adults. Lancet 2003;361(9354):323–31.
[3] Tien RD, Felsberg GJ, Friedman H, Brown M, MacFall J. MR imaging of high-grade cerebral gliomas: value of diffusion-weighted echoplanar pulse sequences. AJR Am J Roentgenol 1994;162(3):671–7.
[4] Yamasaki F, Kurisu K, Satoh K, et al. Apparent diffusion coefficient of human brain tumors at MR imaging. Radiology 2005;235(3):985–91.
[5] Bulakbasi N, Guvenc I, Onguru O, Erdogan E, Tayfun C, Ucoz T. The added value of the apparent diffusion coefficient calculation to magnetic resonance imaging in the differentiation and grading of malignant brain tumors. J Comput Assist Tomogr 2004;28(6):735–46.
[6] Kono K, Inoue Y, Nakayama K, et al. The role of diffusion-weighted imaging in patients with brain tumors. AJNR Am J Neuroradiol 2001;22(6):1081–8.
[7] Kitis O, Altay H, Calli C, Yunten N, Akalin T, Yurtseven T. Minimum apparent diffusion coefficients in the evaluation of brain tumors. Eur J Radiol 2005;55(3):393–400.
[8] Oh J, Henry RG, Pirzkall A, et al. Survival analysis in patients with glioblastoma multiforme: predictive value of choline-to-N-acetylaspartate index, apparent diffusion coefficient, and relative cerebral blood volume. J Magn Reson Imaging 2004;19(5):546–54.
[9] Higano S, Yun X, Kumabe T, et al. Malignant astrocytic tumors: clinical importance of apparent diffusion coefficient in prediction of grade and prognosis. Radiology 2006;241(3):839–46.
[10] Murakami R, Sugahara T, Nakamura H, et al. Malignant supratentorial astrocytoma treated with postoperative radiation therapy: prognostic value of pretreatment quantitative diffusion-weighted MR imaging. Radiology 2007;243(2):493–9.
[11] Sugahara T, Korogi Y, Kochi M, et al. Usefulness of diffusion-weighted MRI with echo-planar technique in the evaluation of cellularity in gliomas. J Magn Reson Imaging 1999;9(1):53–60.
[12] Gupta RK, Sinha U, Cloughesy TF, Alger JR. Inverse correlation between choline magnetic resonance spectroscopy signal intensity and the apparent diffusion coefficient in human glioma. Magn Reson Med 1999;41(1):2–7.
[13] Guo AC, Cummings TJ, Dash RC, Provenzale JM. Lymphomas and high-grade astrocytomas: comparison of water diffusibility and histologic characteristics. Radiology 2002;224(1):177–83.
[14] Gauvain KM, McKinstry RC, Mukherjee P, et al. Evaluating pediatric brain tumor cellularity with diffusion-tensor imaging. AJR Am J Roentgenol 2001;177(2):449–54.
[15] Lyng H, Haraldseth O, Rofstad EK. Measurement of cell density and necrotic fraction in human melanoma xenografts by diffusion weighted magnetic resonance imaging. Magn Reson Med 2000;43(6):828–36.
[16] Lacroix M, Abi-Said D, Fourney DR, et al. A multivariate analysis of 416 patients with glioblastoma multiforme: prognosis, extent of resection, and survival. J Neurosurg 2001;95(2):190–8.
[17] Huisman TA, Loenneker T, Barta G, et al. Quantitative diffusion tensor MR imaging of the brain: field strength related variance of apparent diffusion coefficient (ADC) and fractional anisotropy (FA) scalars. Eur Radiol 2006;16(8):1651–8.
[18] Sasaki M, Yamada K, Watanabe Y, et al. Variability in absolute apparent diffusion coefficient values across different platforms may be substantial: a multivendor, multi-institutional comparison study. Radiology 2008;249(2):624–30.
[19] Engelter ST, Provenzale JM, Petrella JR, DeLong DM, MacFall JR. The effect of aging on the apparent diffusion coefficient of normal-appearing white matter. AJR Am J Roentgenol 2000;175(2):425–30.
[20] Nusbaum AO, Tang CY, Buchsbaum MS, Wei TC, Atlas SW. Regional and global changes in cerebral diffusion with normal aging. AJNR Am J Neuroradiol 2001;22(1):136–42.
[21] Abe O, Aoki S, Hayashi N, et al. Normal aging in the central nervous system: quantitative MR diffusion-tensor analysis. Neurobiol Aging 2002;23(3):433–41.

Endogenous tenascin-C enhances glioblastoma invasion with reactive change of surrounding brain tissue

Eishu Hirata,[1,2] Yoshiki Arakawa,[1,5] Mitsuaki Shirahata,[1] Makoto Yamaguchi,[1] Yo Kishi,[1] Takashi Okada,[1] Jun A. Takahashi,[3] Michiyuki Matsuda[2] and Nobuo Hashimoto[4]

[1]Department of Neurosurgery, [2]Department of Pathology and Biology of Diseases, Kyoto University Graduate School of Medicine, Kyoto 606-8507; [3]Department of Neurosurgery, Kitano Hospital, Osaka 530-8480; [4]National Cardiovascular Center, Osaka 565-8565, Japan

(Received November 25, 2008/Revised March 27, 2009/Accepted April 6, 2009)

Tenascin-C is an extracellular matrix glycoprotein implicated in embryogenesis, wound healing and tumor progression. We previously revealed that tenascin-C expression is correlated with the prognosis of patients with glioblastoma. However, the exact role of endogenous tenascin-C in regulation of glioblastoma proliferation and invasion remains to be established. We show here that endogenous tenascin-C facilitates glioblastoma invasion, followed by reactive change of the surrounding brain tissue. Although shRNA-mediated knockdown of endogenous tenascin-C does not affect proliferation of glioblastoma cells, it abolishes cell migration on a two-dimensional substrate and tumor invasion with brain tissue changes in a xenograft model. The tyrosine phosphorylation of focal adhesion kinase, a cytoplasmic tyrosine kinase that associates with integrins, was decreased in tenascin-C-knockdown cells. In the analysis of clinical samples, tenascin-C expression correlates with the volume of peritumoral reactive change detected by magnetic resonance imaging. Interestingly, glioblastoma cells with high tenascin-C expression infiltrate brain tissue in an autocrine manner. Our results suggest that endogenous tenascin-C contributes the invasive nature of glioblastoma and the compositional change of brain tissue, which renders tenascin-C as a prime candidate for anti-invasion therapy for glioblastoma. (*Cancer Sci* 2009)

Glioblastoma is the most common and most agressive primary brain tumor in adults. As it is recalcitrant to any current treatment including surgery, radiotherapy and chemotherapy, the median survival time is less than 1 year.[1] Glioblastoma is characterized by extensive invasiveness into the surrounding brain tissue, which makes it impossible to provide a cure by surgical resection.[2] For these reasons, recurrent tumors develop adjacent to the resection cavity and in the contralateral hemisphere. Magnetic resonance (MR) imaging is the standard clinical examination for the diagnosis of glioblastoma. Glioblastoma is a radiologically heterogeneous tumor with severe edema of the brain parenchyma. Gadolinium enhancement often demonstrates 'ring enhancement', which represents central necrosis and enhancing rim of glioblastoma cells, with accompanying microvascular hyperplasia and increased permeability.[3] The fluid-attenuated inversion recovery (FLAIR) sequence yields heavily T2-weighted MR images of the brain with suppression of the cerebrospinal fluid signal. Glioblastoma induces vasogenic edema and changes the composition of brain parenchyma. As a possible mechanism, glioblastoma-derived factors downregulate endothelial tight junction proteins, resulting in impairment of the blood–brain barrier.[4] Various extracellular matrices, such as matrix metalloproteinase (MMP), collagen type IV and laminin are increased.[5] For these reasons, FLAIR images can detect the peritumoral change in brain tissue as hyperintense.[6]

This invasive capacity of glioma cells is driven by complex molecular processes involving the remodeling of extracellular matrix (ECM), intracellular signaling and cytoskeletal reorganization.[7] Several genes involved in glioma invasiveness have been identified, including those coding for chemoattractants, signaling molecules, adhesion molecules and MMP.[8–10] Migration of glioma cells involves active intracellular signaling with molecules such as PI3 K, focal adhesion kinase (FAK) and small GTPase proteins.[11] For example, the Rho GTPase RhoA and its effector, mDia1, regulate cell polarity and focal adhesion turnover in migrating glioma cells by localizing adenomatous polyposis coli (Apc) and proto-oncogene-encoded c-Src tyrosine kinase (c-Src).[12] Src binding to FAK contributes to src activation, promoting further phosphorylation of FAK at additional tyrosines, which is responsible for efficient disassembly of focal adhesion.[13] Meanwhile, glioma invasion requires the detachment of the cell from the ECMs and/or the adjacent cells as well as proteolytic degradation of ECMs around the tumor.[2]

Tenascin-C, a component of the ECMs, is highly expressed in many malignancies, including glioblastoma.[14–17] Many previous reports have provided important insights into the biological function of tenascin-C. However, the mechanisms by which it signals are not yet clear, and these appear to be variable across cell types and experimental models.[14] In addition, most studies have relied upon exogenous tenascin-C and *in vitro* models,[18–22] while few have focused upon this protein *in vivo*. Curiously, melanoma invasion *in vivo* was only slightly promoted in knockout mice lacking tenascin-C.[23]

In this study, therefore, we investigated the role of endogenous tenascin-C in glioblastoma invasion and proliferation by using shRNA-mediated knockdown of its expression. To characterize the function of intrinsic tenascin-C of glioblastoma cells *in vivo*, we used a glioblastoma xenograft model. In the analysis of resected tumor in patients with glioblastoma, we examined the correlation between tenascin-C expression, glioblastoma invasion and secondary tissue change of brain parenchyma. Our results provide a new insight into the role of endogenous tenascin-C in glioblastoma progression.

Materials and Methods

Antibodies and reagents. The following primary and secondary antibodies were used for Western blot analysis, immunocytochemistry or immunohistochemistry: anti-human tenascin-C mouse monoclonal antibody (Abcam, Cambridge, MA), anti-human/

[5]To whom correspondence should be addressed.
E-mail: yarakawa@sb3.so-net.ne.jp

doi: 10.1111/j.1349-7006.2009.01189.x

mouse tenascin-C rat monoclonal antibody (R&D Systems, Inc., Minneapolis, MN); anti-human tenascin-C mouse monoclonal antibody (clone 49; Novocastra Laboratories, Newcastle, UK); anti-human Ki-67 mouse monoclonal antibody (clone MM1, Novocastra Laboratories); anti-human α-tubulin mouse monoclonal antibody (TU-02; Santa Cruz Biotechnology, Santa Cruz, CA); anti-phosphotyrosine mouse monoclonal antibody (4G10) (Millipore Corporate Headquarters, Billerica, MA); anti-phosphotyrosine mouse monoclonal (P-Tyr-100) anti-phospho-p130 CAS (Tyr165) rabbit polyclonal antibodies (Cell Signaling Technology, Beverly, MA); anti-p130 CAS, anti-FAK (clone 77) and anti-phospho-FAK (pY397) mouse monoclonal antibodies (BD Bioscience, San Jose, CA); and AlexaFluora 405-goat anti-mouse and 546-goat anti-rat IgG antibodies (Invitrogen, Carlsbad, CA). Rhodamine-conjugated phalloidin (Invitrogen) was used to stain F-actin.

Cell culture. LN229 human glioblastoma cells were obtained from the American Type Culture Collection (Manassas, VA) and maintained in Dulbecco's modified Eagle's medium (DMEM) containing 10% fetal bovine serum (FBS) at 37°C in a humidified atmosphere containing 5% CO_2. For the evaluation of cell growth, 5×10^4 glioma cells were seeded onto 24-well plates, and the number of viable cells was counted on days 2 and 4.

Lentiviral shRNA-mediated RNA interference. The knockdown vector was constructed by using a shRNA expression lentiviral vector. Lentiviral production and infection were described previously.[24] The target sequence for RNA interference was selected from human tenascin-C candidate sequences that are available from GenomeWide siRNA (Qiagen, Hilden, Germany). The selected target sequence for tenascin-C corresponded to the mRNA of the coding region, nt 3853–3871, 5′-GCTGGGAT GCCCTCAAACT-3′. The sequence 5′-GATTCTCCGAACG TGTCAC-3′ was used as a negative control.

Fluorescence microscopy and image analysis. Our method of fluorescence microscopy is described previously.[25] Glioma cells were cultured on non-coated and fibronectin-coated glass-bottom dishes in DMEM with 10% FBS at 37°C in a humidified atmosphere containing 5% CO_2. After 24 h, cells were fixed with 4% paraformaldehyde, permeabilized with 0.2% Triton X-100 in PBS, blocked with 5% BSA and 1% FBS in PBS, and incubated with the primary antibody overnight, followed by incubation with fluorophore-conjugated secondary antibodies. After rinsing in PBS, the cells were imaged with a confocal laser scanning microscope (FV1000; Olympus, Tokyo, Japan). To compare the level of tyrosine phosphorylation at the focal adhesion, the area and intensity of the phospho-tyrosine signal at focal adhesions were measured and corrected by MetMorph software (Molecular Devices, Sunnyvale, CA). The analyses were in the control (3980 focal adhesions in 30 cells) and the tenascin-C knockdown (5072 focal adhesions in 36 cells).

Western blot analysis. Cultured cells at 80% confluency were washed with PBS and the cellular proteins were extracted in cell lysis buffer (Invitrogen) supplemented with 2.5% 2-mercaptoethanol and boiled at 95°C for 5 min. Equal amounts of proteins were electrophoresed in 4–12% precasted Tris-Bis gels (Invitrogen) and transferred onto nitrocellulose membranes with the use of the Iblot system (Invitrogen). After blocking with 5% bovine serum albumin (BSA) in Tris-buffered saline (TBS) with 0.05% Tween 20 (TBS–T), the membrane was incubated with primary antibody overnight at 4°C, followed by washing in TBS–T and incubation with a horseradish peroxidase-conjugated goat anti-mouse IgG diluted in TBS–T with 5% skim milk for 1 h at room temperature. The labeled proteins were visualized with ECL plus Western blot detection system (GE Healthcare, Piscataway, NJ).

Monolayer wound healing assay and cell locomotion assay. A wound was made by scratching the monolayer cells with a pipette tip.[12] After the removal of scratched cells, the cells were cultured for 14 h. Photographs of cells were taken before and after wounding to measure the width of the wound. For the analysis of single cell locomotion, cells were seeded onto either a non-coated or tenascin-C coated (10 μg/mL) glass-bottom dish 24 h before imaging. Cells were imaged every 5 min for 12 h with an Olympus IX81 inverted microscope (Olympus) equipped with the ZDC autofocusing system. Cell track and velocity were calculated with MetMorph software.

Mouse xenograft glioma model. Animal care and experiments complied with Japanese community standards on the care and use of laboratory animals. For intracranial transplantation, glioma cells (5×10^5 cells/5 μL of PBS) were stereotactically transplanted into the right striatum of 9-week-old-male nude mice (BALB/cAJc1-nu) as described elsewhere.[26] Neurological defects and emaciation of the mice were carefully observed every day. Three weeks after transplantation, the brain specimens were prepared after euthanasia. The brain tissues were fixed in 4% paraformaldehyde in PBS. Sectioned coronally at the point of cellular implantation, the brain tissue was embedded into Optimal Cutting Temprature (O.C.T.) compound (Sakura, Tokyo, Japan) and frozen in liquid nitrogen. Twenty-micrometer sections were cut and mounted on silane-coated slides, and observed through a fluorescence microscope system (BX51N-34-FL-1; Olympus).

Resected glioblastoma samples, quantitative reverse transcription PCR (RT-PCR) and immunohistochemistry. Histological diagnosis was conducted according to the WHO Classification of Brain Tumors.[1] Tumor specimens for molecular research were snap-frozen immediately after surgical resection and kept at –80°C. For the sampling of tumor tissues corresponding to the gadolinium-enhanced lesion or hyperintense area of FLAIR sequences, we used either StealthStation TRIA plus with Cranial v4.0 software (Medtronic Sofamor-Danek), or Vector Vision Compact Navigation System with VV Cranial v7.5 software (BrainLab AG, Heim Stetten, Germany). The study protocol was approved by the institutional review board of Kyoto University, and written informed consent was obtained from each patient. For the immunohistochemical analysis in resected glioblastoma samples, the conventional avidin–biotin–peroxidase complex method was used as described elsewhere.[27] For quantitative reverse RT-PCR, we used methods described previously.[28] The second-derivative maximum method was used for crossing-point determination using LightCycler Software 3.3 (Roche, Basel, Switzerland). GAPDH was used as an internal control. The following primer sets were used: forward, 5′-GTCACCGTGTCAACCTGATG-3′, and reverse, 5′-GCCTGCCTTCAAGATTTCTG-3′, for tenascin-C; forward, 5′-TGACAACAGCCTCAAGATCA-3′, and reverse, 5′-CTGTGGTCATGAGTCCTTCC-3′, for GAPDH. The conditions for PCR were 45 cycles of 95°C for 10 s for denaturation, 56°C for 5 s for annealing and 72°C for 10 s for extension.

Measurement of tumor volume and definition of 'FLAIR/Enhanced volume ratio'. To calculate 'FLAIR/Enhanced volume ratio' in each patient, we defined two tumor volumes on the multislice MR images. For measurement of 'Enhanced tumor volume', the border of the tumor area was determined at the enhancing rim on the T1-weighted images with gadolinium enhancement. For measurement of 'FLAIR hyperintensity volume', the border of the tumor area was determined at the outer rim of the hyperintensity area in FLAIR sequences. The planar dimension was analyzed using NIH Image software. In either case, tumor volumes were calculated by the formula: Σ([planar dimension] × [slice distance]). 'FLAIR/Enhanced volume ratio' was defined by the formula: ([FLAIR tumor volume] – [gadolinium-enhanced tumor volume])/[gadolinium-enhanced tumor volume]) (%).

Statistical analysis. The Spearman rank correlation test was used to analyze correlations between tenascin-C expression and Invasion Index. When two groups were compared, an unpaired Student's *t*-test was applied.

doi: 10.1111/j.1349-7006.2009.01189.x

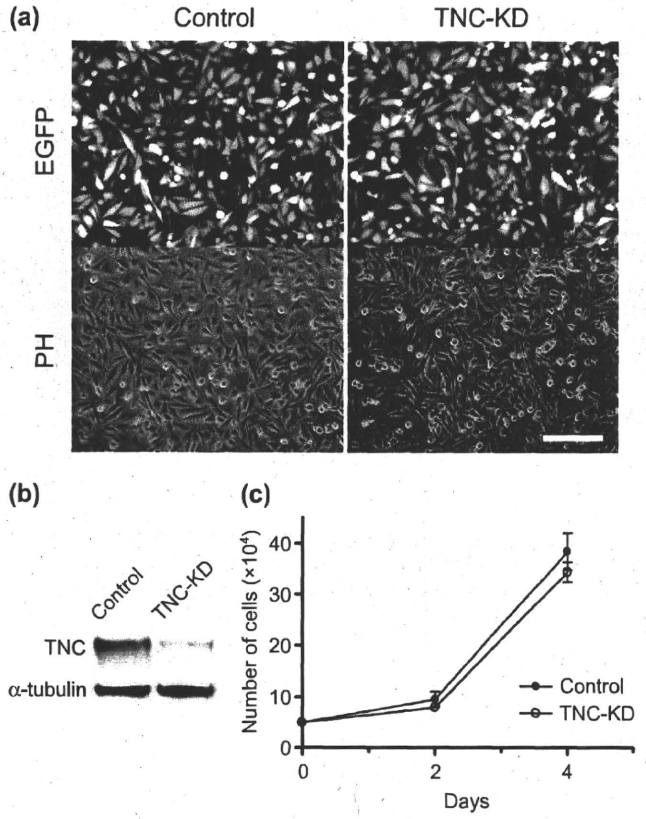

Fig. 1. shRNA-mediated knockdown of tenascin-C does not affect cell proliferation in LN229 glioblastoma cells. (a) Lentiviral shRNA against control and tenascin-C was introduced into LN229 cells and IRES-mediated EGFP expressions were seen as an infection marker. Fluorescence (EGFP) and phase-contrast (PH) images are shown. (b) Representative immunoblot of tenascin-C and α-tubulin in shRNA-mediated protein knockdown against control and tenascin-C in LN229 cells. (c) Quantification of cell growth in control and tenascin-C knockdown cells 2 and 4 days after cell plating. Data are shown as mean ± SD ($n = 3$). Scale bar, 200 μm; TNC-KD, tenascin-C-knockdown cells.

Results

shRNA-mediated knockdown of endogenous tenascin-C does not affect glioblastoma cell proliferation. The biological functions of tenascin-C have been implicated in tumor progression.[29] However, relevant studies to date have been performed using exogenous tenascin-C. To examine the role of endogenous tenascin-C in glioblastoma cells, LN229 cells were transduced with a lentiviral shRNA sequence against tenascin-C to knock down this protein's expression. The lentiviral transduction efficiencies of tenascin-C shRNA and control shRNA were consistently greater than 90% as measured by IRES-mediated enchanced-green fluorescent protein (EGFP) expression (Fig. 1a). Tenascin-C is highly expressed in LN229 cells, and the shRNA for tenascin-C significantly reduced its protein expression (Fig. 1b). Although tenascin-C has been shown to mediate its effects on cell proliferation via mitogen-activated protein kinase signaling in cells plated on fibronectin,[20] there was no significant difference in the growth rates between the control shRNA and the tenascin-C-knockdown glioblastoma cells on the substrata without fibronectin (Fig. 1c). This observation indicates that endogenous tenascin-C does not accelerate cell growth.

Endogenous tenascin-C regulates cell motility in LN229 glioblastoma cells. Addition of extrinsic tenascin-C promotes glioma cell migration and invasion.[18] We tested whether endogenous tenascin-C expression is similarly involved in glioma cell motility, and found that tenascin-C knockdown inhibited glioma cell migration in the monolayer wound healing assay (Fig. 2a,b). Cell migration requires remodeling of the actin cytoskeleton and assembly and disassembly of focal adhesions.[12] For this reason, we hypothesized that endogenous tenascin-C knockdown alters cell adhesion, resulting in diminished cell motility. We examined the cytoskeletons induced by endogenous tenascin-C knockdown. On the fibronectin, the formation of focal adhesion is decreased in the control cells, but it was not clearly changed in tenascin-C-knockdown cells, which is consistent with that of past studies. Interestingly, tyrosine phosphorylation of focal adhesion is decreased in tenascin-C-knockdown cells on non-coated coverslips (Fig. 2c–e). It has been reported that tenascin-C suppresses RhoA activity and inhibits the formation of actin stress fibers.[30] Therefore, we examined the involvement of RhoA in this effect on cell migration; however, no apparent difference was detected in GTP-RhoA (active form of RhoA) (data not shown). In focal adhesions, FAK and p130 Cas (Crk-associated substrate) colocalize with integrins.[13] We found that tyrosine phosphorylation of FAK, but not p130 Cas, was decreased in tenascin-C-knockdown cells. When we analyzed the LN229 cell locomotion by cell-tracking analysis, tenascin-C knockdown glioma cells significantly decreased the mean velocity and the distance from the origin. Another question was whether or not cytoplasmic tenascin-C can act directly on cell motility. Strikingly, coating the tissue culture dishes with tenascin-C restored the migration velocity of the tenascin-C knockdown cells to the level of the parent cells (Fig. 3), which indicates that tenascin-C regulates glioblastoma cell migration in an autocrine manner.

Tenascin-C-knockdown decreases glioblastoma cell invasiveness and reactive change of peritumoral brain tissue. We next examined whether endogenous tenascin-C is involved in glioblastoma cell invasion *in vivo*. We used a xenograft model implanting control and tenascin-C-knockdown LN229 cells into the striatum of BALB/c nude mice. Using this model, we evaluated the invasiveness of glioblastoma cells 3 weeks after implantation. Control shRNA cells exhibited tumor growth and infiltration into the surrounding brain tissue, forming small tumor clusters distinct from the tumor core (Fig. 4a,c). Histopathologically, edematous change was observed in the brain parenchyma containing glioblastoma infiltration (Fig. 4b). Intercellular tenascin-C was also diffusely deposited not only in the tumor core but also in the surrounding brain tissue with glioblastoma cell infiltration (Fig. 4d). In contrast, although tumor size of tenascin-C-knockdown LN229 cell was approximately equal to that of control cells (Fig. 4i), the number of infiltrating glioma cells and tumor clusters in the surrounding brain were decreased (Fig. 4g). As expected, these cells deposited significantly less tenascin-C than the control (Fig. 4h), and the edematous change was decreased in the brain parenchyma around the tumor (Fig. 4f). The infiltrating control cells show dense cytoplasmic tenascin-C (Fig. 4c,d, white rectangles). Quantification of tumor cluster number revealed that tenascin-C knockdown decreased cluster formation by approximately half, compared with control cells (Fig. 4j). These results indicate that endogenous tenascin-C promotes glioblastoma cell invasion and the adjacent reactive change of the brain parenchyma but is not involved in tumor growth in the glioblastoma xenograft models.

Tenascin-C expression correlates with the volume of the reactive brain tissue in glioblastoma. Our experimental study showed that endogenous tenascin-C promotes glioblastoma invasion and a secondary reactive change of the peritumoral tissue. The reactive change of brain tissue contains vasogenic edema and compositional change of brain tissue induced by tumor cell infiltration. In modern MR imaging, the tumor core is enhanced by gadolinium and the peritumoral change in brain parenchyma is seen as a

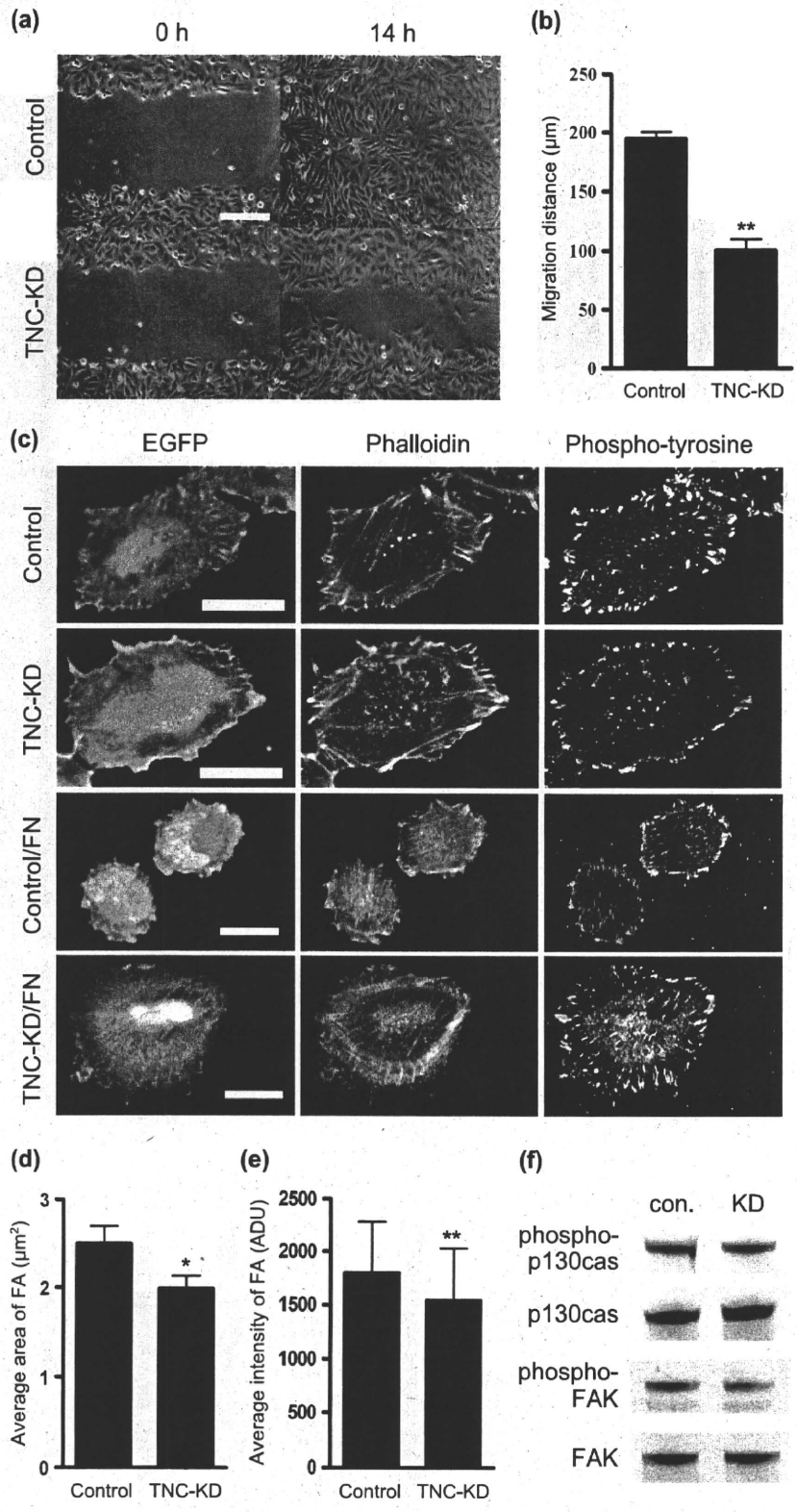

Fig. 2. Endogenous tenascin-C regulates cell motility in LN229 glioblastoma cells. (a) The confluent monolayers of the control and tenascin-C-knockdown LN229 cells were photographed 0 and 14 h after scraping. (b) The distance of cell-edge movements 14 h after scraping is shown as mean ± SD ($n = 3$). (c) F-actin (phalloidin) and tyrosine-phosphorylated proteins were stained in the control and tenascin-C-knockdown cells on the non-coated and fibronectin coated coverslips. (d,e) The average area and intensity of tyrosine-phosphorylation signals in the control and tenascin-C knockdown cells stained by phosphor-tyrosine antibody on the non-coated glass-bottom dishes are measured and shown as mean ± SE (control, $n = 30$; TNC-KD, $n = 36$). (f) Representative immunoblot of phosphorylated p130Cas and FAK in shRNA-mediated protein knockdown against control and tenascin-C in LN229 cells. TNC-KD, tenascin-C-knockdown cells; **, $P < 0.001$; scale bar, 200 μm.

hyperintense region by FLAIR sequences (Fig. 5a). It is therefore possible that the peritumoral hyperintensity area represents the secondary change induced by tenascin-C-facilitated glioblastoma cell invasion. We examined the correlation between the FLAIR/Enhanced volume (F/E) ratio (indicating the volume of peritumoral tissue change), with tenascin-C mRNA expression in resected tumors from 16 glioblastoma patients. Strikingly, tenascin-C expression significantly correlates with

doi: 10.1111/j.1349-7006.2009.01189.x

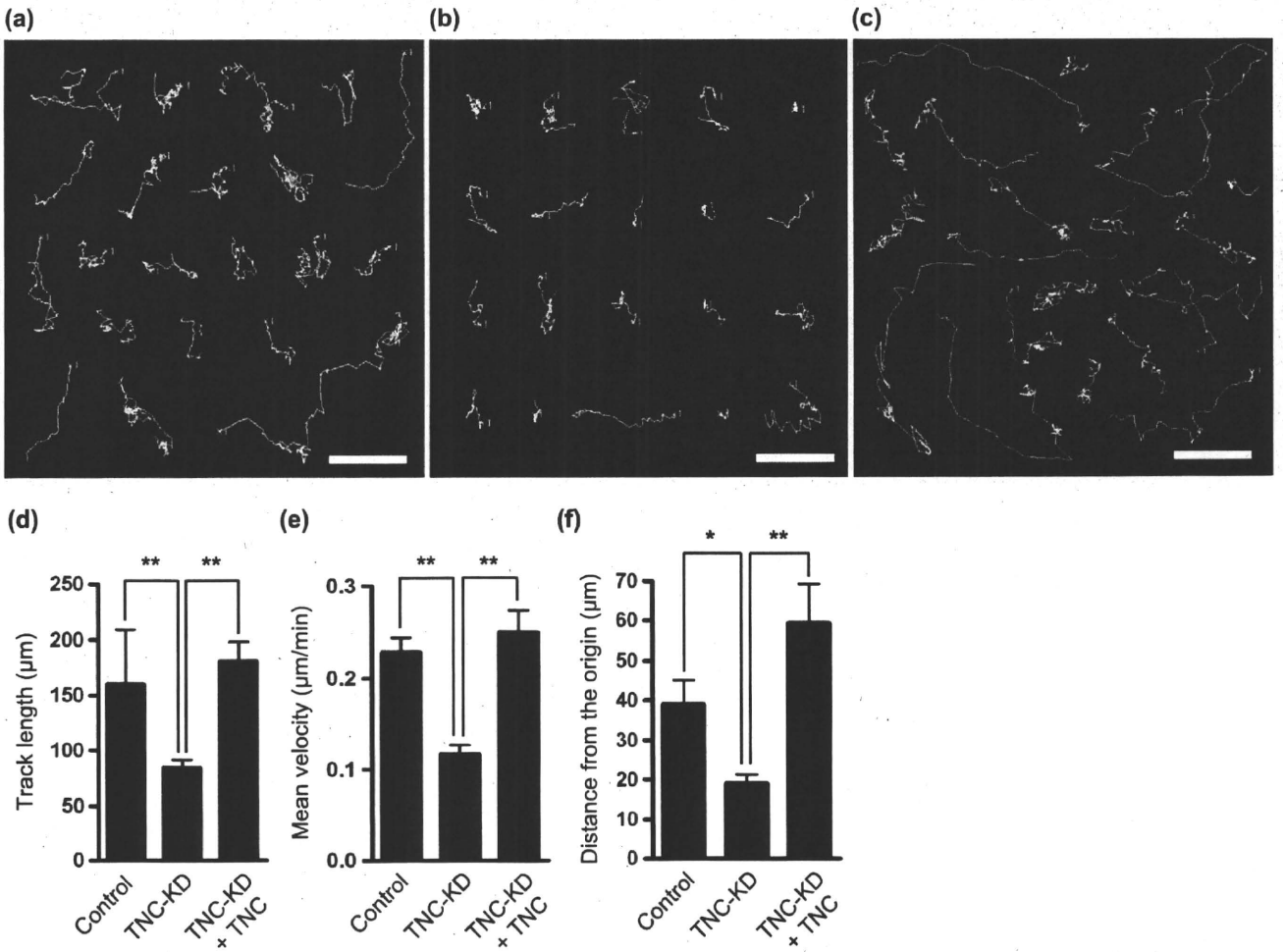

Fig. 3. Endogenous tenascin-C activates glioblastoma cell locomotion. Cell tracking of (a) control cells, (b) tenascin-C-knockdown cells and (c) tenascin-C-knockdown with addition of exogenous tenascin-C. Cells were imaged every 5 min for 12 h under microscopy. (d) Track length (μm). (e) Mean velocity (μm/min). (f) Distance from the origin. Tracks and velocities were calculated with MetMorph software (Molecular Devices, Sunnyvale, CA). TNC-KD, tenascin-C-knockdown cells; TNC-KD + TNC, tenascin-C-knockdown cells with exogenous tenascin-C; *, $P < 0.01$; **, $P < 0.001$; scale bars, 50 μm.

the volume of the peritumoral tissue change (Spearman correlation test, $P = 0.005$, $r = 0.77$) (Fig. 5b), although it does not correlate with the proliferation index by a mitotic marker Ki-67 staining (Spearman correlation test, $P = 0.272$, $r = -0.29$) (Fig. 5c).

The localization of tenascin-C in resected glioblastomas has been described in the perivascular and intercellular spaces. However, it is unclear to what extent tenascin-C is expressed around the tumor.[31] We therefore examined the localization of tenascin-C in resected glioblastoma sections obtained from either the tumor core (gadolinium-enhanced area) or the surrounding lesion (hyperintensity area of FLAIR imaging) by using intraoperative navigation systems. In patients with high and low F/E ratios, intercellular deposition of tenascin-C was detected in the tumor core (Fig. 6a,b, upper panels, TNC). The peritumoral brain parenchyma, showing hyperintensity with FLAIR imaging, contained glioblastoma cells undergoing mitosis (Fig. 6a,b, lower panels, Ki-67). In the patient with a high F/E ratio, a number of glioblastoma cells infiltrated in the peritumoral brain tissue and exhibited high deposition of tenascin-C in their cytoplasm (Fig. 6b, lower panels). Based on these results, one possible mechanism of glioblastoma progression is that glioblastoma infiltration into the brain parenchyma is enhanced by overexpression of endogenous tenascin-C, which induces reactive changes of the brain tissues, detected as hyperintensity area with FLAIR sequences.

Discussion

Numerous studies have revealed that tenascin-C plays a certain role in tumor progression including tumorigenesis, proliferation, invasion, metastasis and angiogenesis.[14,15,18,19,22,32–38] It is widely acknowledged that tenascin-C disrupts the binding of fibronectin to the integrin $\alpha_5\beta_1$/syndecan-4 complex at the cell surface, which causes morphological change of cultured cells and promotes cell proliferation.[22,39,40] However, in this study, no significant differences exist in cell morphology or proliferation between the control and tenascin-C-knockdown glioblastoma cells. This is possibly because tenascin-C affects cell growth and morphology in an environment containing extrinsic tenascin-C and fibronectin.[20,33] While collagen, fibronectin and laminin are the predominant ECM components in non-central nervous system tissue, major ECM components of brain parenchyma include hyaluronan, proteoglycans and glycosaminoglycans, such as hyaluronic acid and chondroitin sulfate. Fibronectin is found at the gliomesenchymal junction of tumors and in tumor-associated blood vessels.[41] Glioblastomas do not express fibronectin, yet fibronectin is confined to proliferating vessel walls and leptomeninges.[42] Fibronectin was either localized in the basement membrane or formed thick, multi-layered deposits in the vessel walls. Fibronectin expression was seen in all glioblastoma samples but

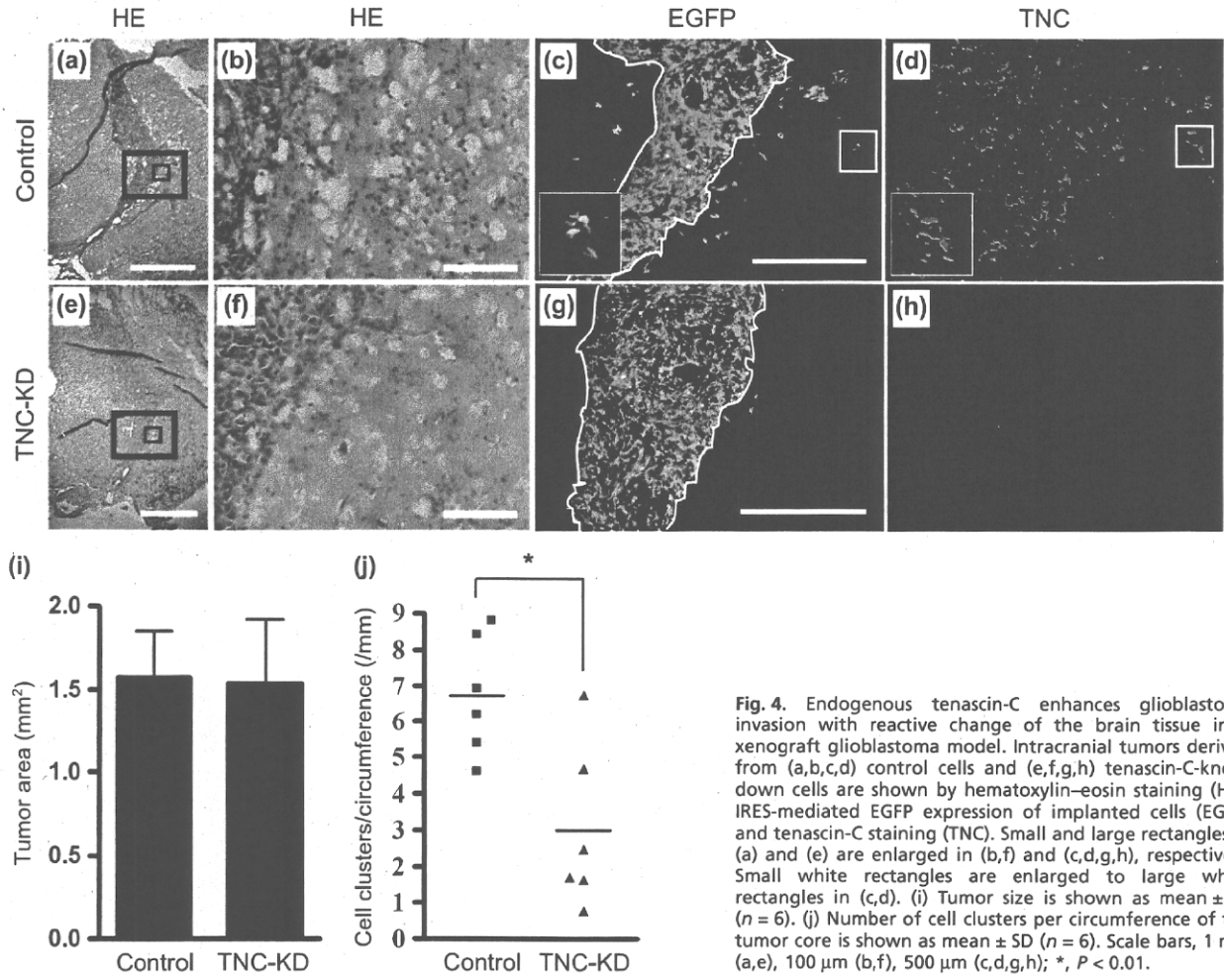

Fig. 4. Endogenous tenascin-C enhances glioblastoma invasion with reactive change of the brain tissue in a xenograft glioblastoma model. Intracranial tumors derived from (a,b,c,d) control cells and (e,f,g,h) tenascin-C-knock down cells are shown by hematoxylin–eosin staining (HE), IRES-mediated EGFP expression of implanted cells (EGFP) and tenascin-C staining (TNC). Small and large rectangles in (a) and (e) are enlarged in (b,f) and (c,d,g,h), respectively. Small white rectangles are enlarged to large white rectangles in (c,d). (i) Tumor size is shown as mean ± SD ($n = 6$). (j) Number of cell clusters per circumference of the tumor core is shown as mean ± SD ($n = 6$). Scale bars, 1 mm (a,e), 100 μm (b,f), 500 μm (c,d,g,h); *, $P < 0.01$.

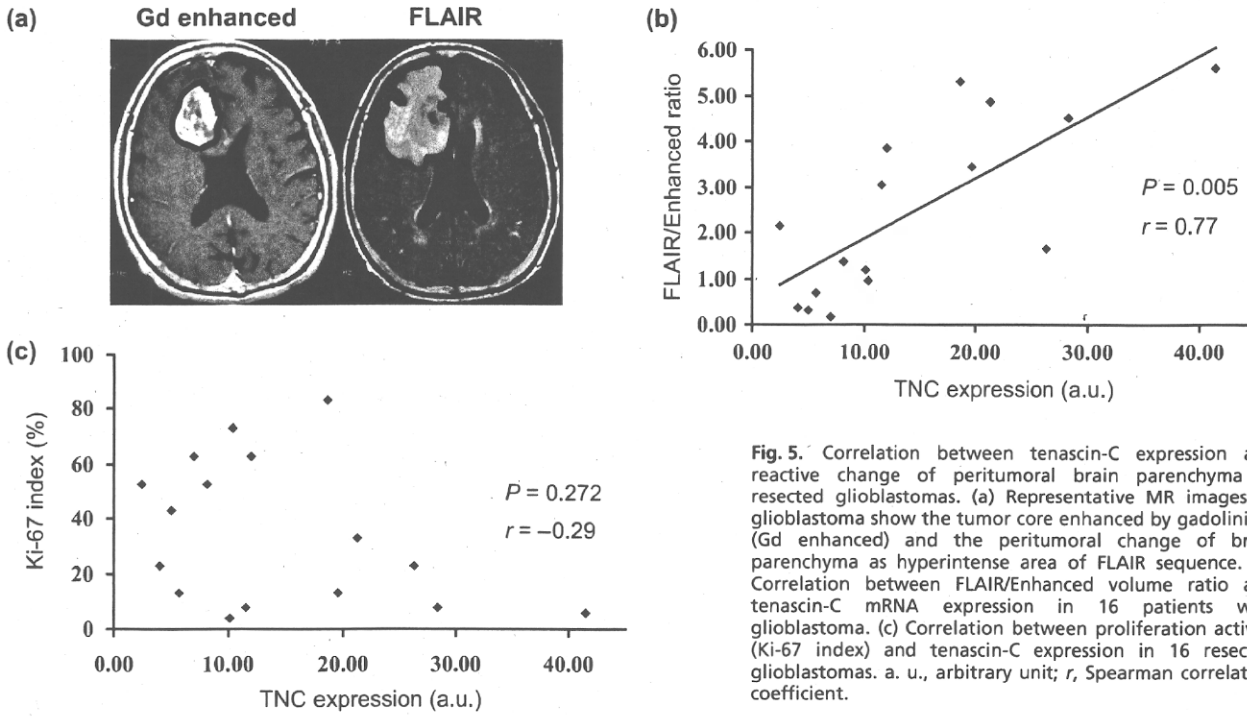

Fig. 5. Correlation between tenascin-C expression and reactive change of peritumoral brain parenchyma in resected glioblastomas. (a) Representative MR images of glioblastoma show the tumor core enhanced by gadolinium (Gd enhanced) and the peritumoral change of brain parenchyma as hyperintense area of FLAIR sequence. (b) Correlation between FLAIR/Enhanced volume ratio and tenascin-C mRNA expression in 16 patients with glioblastoma. (c) Correlation between proliferation activity (Ki-67 index) and tenascin-C expression in 16 resected glioblastomas. a. u., arbitrary unit; *r*, Spearman correlation coefficient.

doi: 10.1111/j.1349-7006.2009.01189.x

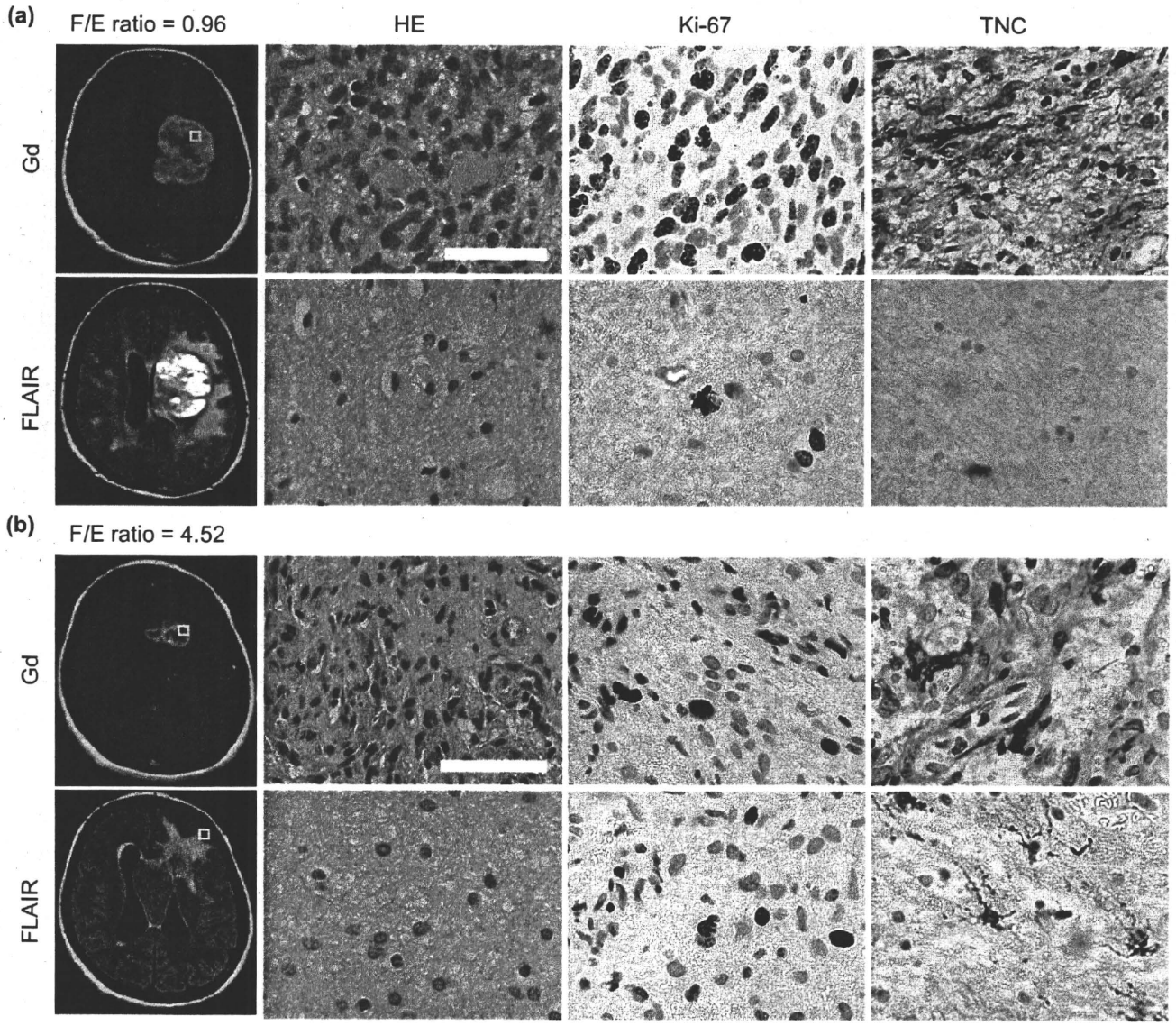

Fig. 6. Infiltrating glioblastoma cells show cytoplasmic deposition of tenascin-C in reactive changes of peritumoral brain parenchyma detected by FLAIR image. Representative images of the tumor core and peritumoral tissue in patients with (a) low FLAIR/Enhanced volume ratio (F/E ratio) and (b) high F/E ratio. Each square in MR images (left panel) indicates the localization of the microscopic images (three right panels; HE, Ki-67, TNC). Hematoxylin–eosin staining (HE), mitotic activity staining (Ki-67), tenascin-C staining (TNC). Scale bars, 200 μm.

its distribution was not uniform, and its staining intensity was weak.[31] These observations suggest that endogenous tenascin-C secreted by glioblastoma cells does not affect cell morphology and proliferation when the tumor microenvironment does not abound in fibronectin.

In this study, glioblastoma cell motility on a non-coated substrate was significantly suppressed in tenascin-C-knockdown cells, indicating that endogenous tenascin-C accelerates glioblastoma cell invasion via different machinery from the action of tenascin-C on fibronectin. The same phenotype was also seen in a xenograft model whereby tenascin-C-knockdown glioblastoma cells exhibited less invasiveness into brain parenchyma. Immunohistochemical localization of tenascin-C *in vivo* experiments and clinical samples demonstrate predominant cytoplasmic deposition in the glioblastoma cells invading into brain tissue, especially in the patient with high F/E ratio, which shows highly invasive tumor. These observations suggest that glioblastoma cells with abundant expression of tenascin-C invade aggressively and secreted tenascin-C acts to enhance their invasiveness in an autocrine manner. Tenascin-C was described as a hexabrachion because it exists as a hexamer of 220–320-kDa subunits. Each subunit of tenascin-C comprises three types of structural modules: EGF-like domains, fibronectin type III (FNIII) repeat domains, and a terminal knob homologous to the beta- and gamma-chains of fibrinogen. This multidomain structure of the tenascin-C suggests the possibility of multiple independent functions.[43] In this study, we confirmed that extrinsic tenascin-C rescued the migration disorder of tenascin-C knockdown cells. It is a possible mechanism that endogenous tenascin-C is involved in the regulation of focal adhesion turnover.

The expression level of tenascin-C correlates with prognosis in patients with many malignancies.[14,37,44–49] In the previous study, we identified tenascin-C expression as prognosis factor of patients with glioblastoma.[9] The invasive nature of gliomas also causes breakdown of the blood–brain barrier and cerebral edema formation, which is responsible for significant morbidity and

mortality in patients with glioblastoma. In this study, we found that the expression level of tenascin-C correlates with the degree of peritumoral change in brain parenchyma. This change in brain parenchyma is thought to be comprised of focal brain edema and changes of extracellular matrix following glioblastoma cell invasion; however, the underlying mechanism is still unclear.

The change of the peritumoral brain tissue is usually detected as hyperintensity in T2-weighted images and FLAIR sequences of MR imaging.[2,3,7] Regrettably, it was impossible to evaluate discriminatively the gadolinium-enhanced tumor core and the peritumoral hyperintensity area in our mouse xenograft model. In the immunohistochemical analysis, diffuse deposition of tenascin-C was observed in the stroma of the tumor core and peritumoral brain tissue. Interestingly, strong cytoplasmic deposition of tenascin-C was detected in the migrating glioblastoma cells at the invasion border and in the peritumoral brain tissue. In a study of breast cancer cells, Ishihara *et al.* emphasized that cancer spreading might be involved in cytoplasmic deposition of tenascin-C, but not in intercellular deposition.[50] Taken together, tenascin-C may be one of the key extracellular matrix components facilitating glioblastoma cell invasion and promoting the peritumoral change of brain parenchyma.

In summary, we report that endogenous tenascin-C facilitates glioblastoma cell invasion by regulating focal adhesion and that glioblastoma cells with high tenascin-C expression exhibit invasive nature. Consistent with these observations, the expression level of tenascin-C correlates with the degree of peritumoral tissue change, detected as FLAIR hyperintensity in clinical samples. The detail molecular basis for this curious ability of endogenous tenascin-C to facilitate glioblastoma cell invasion is still unclear and warrants further investigation. This study highlights tenascin-C's attractiveness as a target molecule for anti-invasion therapy in the treatment of glioblastoma.

Acknowledgments

We thank M Way (Cancer Research UK, London) for reagents. We thank members of Arakawa's and Matsuda's laboratories for constructive comments on the manuscript and throughout the project. This work was supported by grants from a Grant-in-Aid for Specially Promoted Research from the Ministry for Education, Culture, Sports, Science and Technology of Japan (YA, YK, JAT, MM, NH), Kyoto University Research Fund (YA) and Japan Heart Foundation/Bayer Yakuhin Research Grant (YA).

Disclosure Statement

We declare that we have no competing financial interests.

References

1 Kleihues P, Burger PC, Scheithauer BW. The new WHO classification of brain tumours. *Brain Pathol* 1993; **3**: 255–68.
2 Nakada M, Nakada S, Demuth T, Tran NL, Hoelzinger DB, Berens ME. Molecular targets of glioma invasion. *Cell Mol Life Sci* 2007; **64**: 458–78.
3 Henson JW, Gaviani P, Gonzalez RG. MRI in treatment of adult gliomas. *Lancet Oncol* 2005; **6**: 167–75.
4 Ishihara H, Kubota H, Lindberg RL *et al.* Endothelial cell barrier impairment induced by glioblastomas and transforming growth factor beta2 involves matrix metalloproteinases and tight junction proteins. *J Neuropathol Exp Neurol* 2008; **67**: 435–48.
5 McKeever PE, Varani J, Papadopoulos SM, Wang M, McCoy JP. Products of cells from gliomas: IX. Evidence that two fundamentally different mechanisms change extracellular matrix expression by gliomas. *J Neurooncol* 1995; **24**: 267–80.
6 Ganslandt O, Stadlbauer A, Fahlbusch R *et al.* Proton magnetic resonance spectroscopic imaging integrated into image-guided surgery: correlation to standard magnetic resonance imaging and tumor cell density. *Neurosurgery* 2005; **56**: 291–8.
7 Claes A, Idema AJ, Wesseling P. Diffuse glioma growth: a guerilla war. *Acta Neuropathol* 2007; **114**: 443–58.
8 Nutt CL, Mani DR, Betensky RA *et al.* Gene expression-based classification of malignant gliomas correlates better with survival than histological classification. *Cancer Res* 2003; **63**: 1602–7.
9 Shirahata M, Iwao-Koizumi K, Saito S *et al.* Gene expression-based molecular diagnostic system for malignant gliomas is superior to histological diagnosis. *Clin Cancer Res* 2007; **13**: 7341–56.
10 Demuth T, Berens ME. Molecular mechanisms of glioma cell migration and invasion. *J Neurooncol* 2004; **70**: 217–28.
11 Furnari FB, Fenton T, Bachoo RM *et al.* Malignant astrocytic glioma: genetics, biology, and paths to treatment. *Genes Dev* 2007; **21**: 2683–710.
12 Yamana N, Arakawa Y, Nishino T *et al.* The Rho-mDia1 pathway regulates cell polarity and focal adhesion turnover in migrating cells through mobilizing Apc and c-Src. *Mol Cell Biol* 2006; **26**: 6844–58.
13 Katz BZ, Romer L, Miyamoto S *et al.* Targeting membrane-localized focal adhesion kinase to focal adhesions: roles of tyrosine phosphorylation and SRC family kinases. *J Biol Chem* 2003; **278**: 29115–20.
14 Orend G, Chiquet-Ehrismann R. Tenascin-C induced signaling in cancer. *Cancer Lett* 2006; **244**: 143–63.
15 Chiquet-Ehrismann R. Tenascins. *Int J Biochem Cell Biol* 2004; **36**: 986–90.
16 Kawakatsu H, Shiurba R, Obara M, Hiraiwa H, Kusakabe M, Sakakura T. Human carcinoma cells synthesize and secrete tenascin in vitro. *Jpn J Cancer Res* 1992; **83**: 1073–80.
17 Sugawara I, Hirakoshi J, Kusakabe M, Masunaga A, Itoyama S, Sakakura T. Relationships among tenascin expression, DNA ploidy patterns, and multidrug resistance gene product (P-glycoprotein) in human colon carcinoma. *Jpn J Cancer Res* 1993; **84**: 703–7.
18 Sarkar S, Nuttall RK, Liu S, Edwards DR, Yong VW. Tenascin-C stimulates glioma cell invasion through matrix metalloproteinase-12. *Cancer Res* 2006; **66**: 11771–80.
19 Zagzag D, Shiff B, Jallo GI *et al.* Tenascin-C promotes microvascular cell migration and phosphorylation of focal adhesion kinase. *Cancer Res* 2002; **62**: 2660–8.
20 Ruiz C, Huang W, Hegi ME *et al.* Growth promoting signaling by tenascin-C [corrected]. *Cancer Res* 2004; **64**: 7377–85.
21 Deryugina EI, Bourdon MA. Tenascin mediates human glioma cell migration and modulates cell migration on fibronectin. *J Cell Sci* 1996; **109** (Pt 3): 643–52.
22 Lange K, Kammerer M, Hegi ME *et al.* Endothelin receptor type B counteracts tenascin-C-induced endothelin receptor type A-dependent focal adhesion and actin stress fiber disorganization. *Cancer Res* 2007; **67**: 6163–73.
23 Matsumoto K, Takahashi K, Yoshiki A, Kusakabe M, Ariga H. Invasion of melanoma in double knockout mice lacking tenascin-X and tenascin-C. *Jpn J Cancer Res* 2002; **93**: 968–75.
24 Rubinson DA, Dillon CP, Kwiatkowski AV *et al.* A lentivirus-based system to functionally silence genes in primary mammalian cells, stem cells and transgenic mice by RNA interference. *Nat Genet* 2003; **33**: 401–6.
25 Arakawa Y, Cordeiro JV, Schleich S, Newsome TP, Way M. The release of vaccinia virus from infected cells requires RhoA-mDia modulation of cortical actin. *Cell Host Microbe* 2007; **1**: 227–40.
26 Candolfi M, Curtin JF, Nichols WS *et al.* Intracranial glioblastoma models in preclinical neuro-oncology: neuropathological characterization and tumor progression. *J Neurooncol* 2007; **85**: 133–48.
27 Toda Y, Kono K, Abiru H *et al.* Application of tyramide signal amplification system to immunohistochemistry: a potent method to localize antigens that are not detectable by ordinary method. *Pathol Int* 1999; **49**: 479–83.
28 Oda M, Arakawa Y, Kano H *et al.* Quantitative analysis of topoisomerase IIalpha to rapidly evaluate cell proliferation in brain tumors. *Biochem Biophys Res Commun* 2005; **331**: 971–6.
29 Chiquet-Ehrismann R, Chiquet M. Tenascins: regulation and putative functions during pathological stress. *J Pathol* 2003; **200**: 488–99.
30 Midwood KS, Schwarzbauer JE. Tenascin-C modulates matrix contraction via focal adhesion kinase- and Rho-mediated signaling pathways. *Mol Biol Cell* 2002; **13**: 3601–13.
31 Oz B, Karayel FA, Gazio NL, Ozlen F, Balci K. The distribution of extracellular matrix proteins and CD44S expression in human astrocytomas. *Pathol Oncol Res* 2000; **6**: 118–24.
32 Behrem S, Zarkovic K, Eskinja N, Jonjic N. Distribution pattern of tenascin-C in glioblastoma: correlation with angiogenesis and tumor cell proliferation. *Pathol Oncol Res* 2005; **11**: 229–35.
33 Huang W, Chiquet-Ehrismann R, Moyano JV, Garcia-Pardo A, Orend G. Interference of tenascin-C with syndecan-4 binding to fibronectin blocks cell adhesion and stimulates tumor cell proliferation. *Cancer Res* 2001; **61**: 8586–94.
34 Mahesparan R, Read TA, Lund-Johansen M, Skaftnesmo KO, Bjerkvig R,

doi: 10.1111/j.1349-7006.2009.01189.x